

Jordan Journal of P H Y S I C S

An International Peer-Reviewed Research Journal

Volume 3, No. 2, 2010, 1432 H

Jordan Journal of Physics (JJP): An International Peer-Reviewed Research Journal established by the Higher Research Committee, Ministry of Higher Education & Scientific Research, Jordan, and published quarterly by the Deanship of Research & Graduate Studies, Yarmouk University, Irbid, Jordan.

EDITOR-IN-CHIEF:

Ibrahim O. Abu Al-Jarayesh

Department of Physics, Yarmouk University, Irbid, Jordan.

ijaraysh@yu.edu.jo

EDITORIAL BOARD:

Dia-Eddin M. Arafah

Department of Physics, University of Jordan, Amman, Jordan.

darafah@ju.edu.jo

Nabil Y. Ayoub

Department of Physics, Yarmouk University, Irbid, Jordan.

nayoub@yu.edu.jo

Hisham B. Ghassib

Princess Sumaya University for Technology, Amman, Jordan.

ghassib@psut.edu.jo

Jamil M. Khalifeh

Department of Physics, University of Jordan, Amman, Jordan.

jkalifa@ju.edu.jo

Sami H. Mahmood

Department of Physics, University of Jordan, Amman, Jordan.

s.mahmood@ju.edu.jo

Marwan S. Mousa

Department of Physics, Mu'tah University, Al-Karak, Jordan.

mmousa@mutah.edu.jo

Nihad A. Yusuf

Department of Physics, Yarmouk University, Irbid, Jordan.

nihadyusuf@yu.edu.jo

Khalaf A. Al-Masaid

Department of Applied Physical Sciences, Jordan University Of Science And Technology, Irbid, Jordan.

khalaf@just.edu.jo

EDITORIAL SECRETARY: Majdi Al-Shannaq.

Manuscripts should be submitted to:

Prof. Ibrahim O. Abu Al-Jarayesh
Editor-in-Chief, Jordan Journal of Physics
Deanship of Research and Graduate Studies
Yarmouk University-Irbid-Jordan
Tel. 00 962 2 7211111 Ext. 2075
E-mail: jjp@yu.edu.jo
Website: <http://Journals.yu.edu.jo/jjp>

Jordan Journal of PHYSICS

An International Peer-Reviewed Research Journal

Volume 3, No. 2, 2010, 1432 H

INTERNATIONAL ADVISORY BOARD

Prof. Dr. Ahmad Saleh

Department of Physics, Yarmouk University, Irbid, Jordan.
salema@yu.edu.jo

Prof. Dr. Aurore Savoy-Navarro

LPNHE Université de Paris 6/IN2P3-CNRS, Tour 33, RdC 4,
Place Jussieu, F 75252, Paris Cedex 05, France.
aurore@lpnhep.in2p3.fr

Prof. Dr. Bernard Barbara

Laboratoire Louis Neel, Salle/Room: D 108, 25, Avenue des
Martyrs BP 166, 38042-Grenoble Cedex 9, France.
Barbara@grenoble.cnrs.fr

Prof. Dr. Bruno Guiderdoni

Observatoire Astronomique de Lyon, g, avenue Ch. Antre-F-69561,
Saint Genis Laval Cedex, France.
Bruno.guiderdoni@olos.univ-lyon1.fr

Prof. Dr. Buford Price

Physics Department, University of California, Berkeley, CA 94720,
U. S. A.
bprice@berkeley.edu

Prof. Dr. Colin Cough

School of Physics and Astronomy, University of Birmingham, B15
2TT, U. K.
c.gough@bham.ac.uk

Prof. Dr. Desmond Cook

Department of Physics, Condensed Matter and Materials Physics
Research Group, Old Dominion University, Norfolk, Virginia
23529, U. S. A.
Dcook@physics.odu.edu

Prof. Dr. Evgeny Sheshin

MIPT, Institutskij per. 9, Dogoprudnyi 141700, Russia.
sheshin@lafeet.mipt.ru

Prof. Dr. Hans Ott

Laboratorium fuer Festkorperphysik, ETH Honggerberg, CH-
8093 Zurich, Switzerland.
ott@solid.phys.ethz.ch

Prof. Dr. Herwig Schopper

President SESAME Council, Chairman Scientific Board UNESCO
IBSP Programme, CERN, 1211 Geneva, Switzerland.
Herwig.Schopper@cern.ch

Prof. Dr. Humam Ghassib

Department of Physics, Jordan University, Amman, Jordan.
humam@atf.org.jo

Prof. Dr. Ingo Hofmann

GSI Darmstadt, Planckstr. 1, 64291, Darmstadt, Germany.
i.hofmann@gsi.de

Prof. Dr. Jozef Lipka

Department of Nuclear Physics and Technology, Slovak University
of Technology, Bratislava, Ilkovicova 3, 812 19 Bratislava,
Slovakia.
Lipka@elf.stuba.sk

Prof. Dr. Khalid Touqan

Chairman of Jordan Atomic Energy Commission, Amman, Jordan.

Prof. Dr. Mark J. Haggmann

Desert Electronics Research Corporation, 762 Lacey Way, North
Salt Lake 84064, Utah, U. S. A.
MHaggmann@NewPathResearch.Com

Prof. Dr. Nasr Zubeidey

President: Al-Zaytoonah University of Jordan, Amman, Jordan.
President@alzaytoonah.edu.jo

Prof. Dr. Patrick Roudeau

Laboratoire de l'Accelérateur, Lineaire (LAL), Université Paris-
Sud 11, Batiment 200, 91898 Orsay Cedex, France.
roudeau@mail.cern.ch

Prof. Dr. Paul Chu

Department of Physics, University of Houston, Houston, Texas
77204-5005, U. S. A.
Ching-Wu.Chu@mail.uh.edu

Prof. Dr. Peter Dowben

Nebraska Center for Materials and Nanoscience, Department of
Physics and Astronomy, 255 Behlen Laboratory (10th and R
Streets), 116 Brace Lab., P. O. Box 880111, Lincoln, NE 68588-
0111, U. S. A.
pdowben@unl.edu

Prof. Dr. Peter Mulser

Institute fuer Physik, T.U. Darmstadt, Hochschulstr. 4a, 64289
Darmstadt, Germany.
Peter.mulser@physik.tu-darmstadt.de

Prof. Dr. Rasheed Azzam

Department of Electrical Engineering, University of New Orleans
New Orleans, Louisiana 70148, U. S. A.
razzam@uno.edu

Dr. Richard G. Forbes

University of Surrey, FEPS (X1), Guildford, Surrey GU2 7XH,
U. K.
R.Forbes@surrey.ac.uk

Prof. Dr. Roy Chantrell

Physics Department, York University, York, YO10 5DD, U. K.
Rc502@york.ac.uk

Prof. Dr. Shawqi Al-Dallal

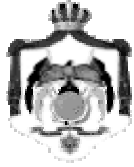
Department of Physics, Faculty of Science, University of Bahrain,
Manamah, Kingdom of Bahrain.

Prof. Dr. Susamu Taketomi

Matsumoto Yushi-Seiyaku Co. Ltd., Shibukawa-Cho, Yao City,
Osaka 581-0075, Japan.
staketomi@hotmail.com

Prof. Dr. Wolfgang Nolting

Institute of Physics / Chair: Solid State Theory, Humboldt-
University at Berlin, Newtonstr. 15 D-12489 Berlin, Germany
Wolfgang.nolting@physik.hu-berlin.de



The Hashemite Kingdom of Jordan



Yarmouk University

Jordan Journal of
PHYSICS
An International Peer-Reviewed Research Journal

Volume 3, No. 2, 2010, 1432 H

Instructions to Authors

Instructions to authors concerning manuscript organization and format apply to hardcopy submission by mail, and also to electronic online submission via the Journal homepage website (<http://jjp.yu.edu.jo>).

Manuscript Submission

1- **Hardcopy:** The original and three copies of the manuscript, together with a covering letter from the corresponding author, should be submitted to the Editor-in-Chief:

Professor Ibrahim O. Abu Al-Jarayesh
Editor-in-Chief, Jordan Journal of Physics
Deanship of Scientific Research and Graduate Studies
Yarmouk University, Irbid, Jordan.
Tel: 00962-2-7211111, Ext. 2075
Fax: 00962-2-7211121
E-mail: jjp@yu.edu.jo

2- **Online:** Follow the instructions at the journal homepage website.

Original *Research Articles*, *Communications* and *Technical Notes* are subject to critical review by minimum of two competent referees. Authors are encouraged to suggest names of competent reviewers. *Feature Articles* in active Physics research fields, in which the author's own contribution and its relationship to other work in the field constitute the main body of the article, appear as a result of an invitation from the Editorial Board, and will be so designated. The author of a *Feature Article* will be asked to provide a clear, concise and critical status report of the field as an introduction to the article. *Review Articles* on active and rapidly changing Physics research fields will also be published. Authors of *Review Articles* are encouraged to submit two-page proposals to the Editor-in-Chief for approval. Manuscripts submitted in *Arabic* should be accompanied by an Abstract and Keywords in English.

Organization of the Manuscript

Manuscripts should be typed double spaced on one side of A4 sheets (21.6 x 27.9 cm) with 3.71 cm margins, using Microsoft Word 2000 or a later version thereof. The author should adhere to the following order of presentation: Article Title, Author(s), Full Address and E-mail, Abstract, PACS and Keywords, Main Text, Acknowledgment. Only the first letters of words in the Title, Headings and Subheadings are capitalized. Headings should be in **bold** while subheadings in *italic* fonts.

Title Page: Includes the title of the article, authors' first names, middle initials and surnames and affiliations. The affiliation should comprise the department, institution (university or company), city, zip code and state and should be typed as a footnote to the author's name. The name and complete mailing address, telephone and fax numbers, and e-mail address of the author responsible for correspondence (designated with an asterisk) should also be included for official use. The title should be carefully, concisely and clearly constructed to highlight the emphasis and content of the manuscript, which is very important for information retrieval.

Abstract: A one paragraph abstract not exceeding 200 words is required, which should be arranged to highlight the purpose, methods used, results and major findings.

Keywords: A list of 4-6 keywords, which expresses the precise content of the manuscript for indexing purposes, should follow the abstract.

PACS: Authors should supply one or more relevant PACS-2006 classification codes, (available at <http://www.aip.org/pacs/pacs06/pacs06-toc.html>)

Introduction: Should present the purpose of the submitted work and its relationship to earlier work in the field, but it should not be an extensive review of the literature (e.g., should not exceed 1 ½ typed pages).

Experimental Methods: Should be sufficiently informative to allow competent reproduction of the experimental procedures presented; yet concise enough not to be repetitive of earlier published procedures.

Results: should present the results clearly and concisely.

Discussion: Should be concise and focus on the interpretation of the results.

Conclusion: Should be a brief account of the major findings of the study not exceeding one typed page.

Acknowledgments: Including those for grant and financial support if any, should be typed in one paragraph directly preceding the References.

References: References should be typed double spaced and numbered sequentially in the order in which they are cited in the text. References should be cited in the text by the appropriate Arabic numerals, enclosed in square brackets. Titles of journals are abbreviated according to list of scientific periodicals. The style and punctuation should conform to the following examples:

1. Journal Article:

- a) Heisenberg, W., *Z. Phys.* 49 (1928) 619.
- b) Bednorz, J. G. and Müller, K. A., *Z. Phys.* B64 (1986) 189
- c) Bardeen, J., Cooper, L.N. and Schrieffer, J. R., *Phys. Rev.* 106 (1957) 162.
- d) Asad, J. H., Hijjawi, R. S., Sakaji, A. and Khalifeh, J. M., *Int. J. Theor. Phys.* 44(4) (2005), 3977.

2. Books with Authors, but no Editors:

- a) Kittel, C., "Introduction to Solid State Physics", 8th Ed. (John Wiley and Sons, New York, 2005), chapter 16.
- b) Chikazumi, S., C. D. Graham, JR, "Physics of Ferromagnetism", 2nd Ed. (Oxford University Press, Oxford, 1997).

3. Books with Authors and Editors:

- a) Allen, P. B. "Dynamical Properties of Solids", Ed. (1), G. K. Horton and A. A. Maradudin (North-Holland, Amsterdam, 1980), p137.
- b) Chantrell, R. W. and O'Grady, K., "Magnetic Properties of Fine Particles" Eds. J. L. Dormann and D. Fiorani (North-Holland, Amsterdam, 1992), p103.

4. Technical Report:

Purcell, J. "The Superconducting Magnet System for the 12-Foot Bubble Chamber", report ANL/HEP6813, Argonne Natl. Lab., Argonne, III, (1968).

5. Patent:

Bigham, C. B., Schneider, H. R., US patent 3 925 676 (1975).

6. Thesis:

Mahmood, S. H., Ph.D. Thesis, Michigan State University, (1986), USA (Unpublished).

7. Conference or Symposium Proceedings:

Blandin, A. and Lederer, P. *Proc. Intern. Conf. on Magnetism, Nottingham* (1964), P.71.

8. Internet Source:

Should include authors' names (if any), title, internet website, URL, and date of access.

9. Prepublication online articles (already accepted for publication):

Should include authors' names (if any), title of digital database, database website, URL, and date of access.

For other types of referenced works, provide sufficient information to enable readers to access them.

Tables: Tables should be numbered with Arabic numerals and referred to by number in the Text (e.g., Table 1). Each table should be typed on a separate page with the legend above the table, while explanatory footnotes, which are indicated by superscript lowercase letters, should be typed below the table.

Illustrations: Figures, drawings, diagrams, charts and photographs are to be numbered in a consecutive series of Arabic numerals in the order in which they are cited in the text. Computer-generated illustrations and good-quality digital photographic prints are accepted. They should be black and white originals (not photocopies) provided on separate pages and identified with their corresponding numbers. Actual size graphics should be provided, which need no further manipulation, with lettering (Arial or Helvetica) not smaller than 8 points, lines no thinner than 0.5 point, and each of uniform density. All colors should be removed from graphics except for those graphics to be considered for publication in color. If graphics are to be submitted digitally, they should conform to the following minimum resolution requirements: 1200 dpi for black and white line art, 600 dpi for grayscale art, and 300 dpi for color art. All graphic files must be saved as TIFF images, and all illustrations must be submitted in the actual size at which they should appear in the journal. Note that good quality hardcopy original illustrations are required for both online and mail submissions of manuscripts.

Text Footnotes: The use of text footnotes is to be avoided. When their use is absolutely necessary, they should be typed at the bottom of the page to which they refer, and should be cited in the text by a superscript asterisk or multiples thereof. Place a line above the footnote, so that it is set off from the text.

Supplementary Material: Authors are encouraged to provide all supplementary materials that may facilitate the review process, including any detailed mathematical derivations that may not appear in whole in the manuscript.

Revised Manuscript and Computer Disks

Following the acceptance of a manuscript for publication and the incorporation of all required revisions, authors should submit an original and one more copy of the final disk containing the complete manuscript typed double spaced in Microsoft Word for Windows 2000 or a later version thereof. All graphic files must be saved as PDF, JPG, or TIFF images.

Allen, P.B., “.....”, in: Horton, G.K., and Muradudin, A. A., (eds.), “Dynamical.....”, (North.....), pp....

Reprints

Twenty (20) reprints free of charge are provided to the corresponding author. For orders of more reprints, a reprint order form and prices will be sent with the article proofs, which should be returned directly to the Editor for processing.

Copyright

Submission is an admission by the authors that the manuscript has neither been previously published nor is being considered for publication elsewhere. A statement transferring copyright from the authors to Yarmouk University is required before the manuscript can be accepted for publication. The necessary form for such transfer is supplied by the Editor-in-Chief. Reproduction of any part of the contents of a published work is forbidden without a written permission by the Editor-in-Chief.

Disclaimer

Opinions expressed in this Journal are those of the authors and neither necessarily reflects the opinions of the Editorial Board or the University, nor the policy of the Higher Scientific Research Committee or the Ministry of Higher Education and Scientific Research. The publisher shoulders no responsibility or liability whatsoever for the use or misuse of the information published by JJP.

Indexing

JJP is currently applying for indexing and abstracting to all related International Services.

Jordan Journal of
P H Y S I C S

An International Peer-Reviewed Research Journal

Volume 3, No. 2, 2010, 1432 H

Table of Contents:

English Articles	Pages
Fractional Canonical Quantization of the Free Electromagnetic Lagrangian Density E. K. Jaradat, R. S. Hijjawi and J. M. Khalifeh	47-54
Comparative Study of the Conductivity Percolation Behaviour of Nanocomposite Thin Layers Made of Nanoparticulate ITO and Carbon Nanotubes Colloids Naji Al Dahoudi	55-60
AFM Study of Multilayer Sol-gel $Ba_xSr_{1-x}TiO_3$ Thin Films Ala'eddin A. Saif, N. Ramli and P. Poopalan	61-68
Ionosphere Scintillation and Earthquakes R. A. Kandalyan and M. Kh. Alquran	69-76
Beryllium Doped <i>p</i>-type GaN Grown by Metal-Organic Chemical Vapor Deposition T. M. Al Tahtamouni, A. Sedhain, J. Y. Lin and H. X. Jiang	77-81
Visibility Degradation and Light Scattering/Absorption Due to Aerosol Particles in Urban/Suburban Atmosphere of Irbid, Jordan Khadeejah M. Hamasha	83-93

Jordan Journal of Physics

ARTICLE

Fractional Canonical Quantization of the Free Electromagnetic Lagrangian Density

E. K. Jaradat^a, R. S. Hijawi^b and J. M. Khalifeh^a

^a *Department of Physics, University of Jordan, 11942 Amman, Jordan.*

^b *Department of Physics, Mutah University, Al-Karak, Jordan.*

Received on: 28/03/2010; Accepted on: 27/6/2010

Abstract: We reformulated the fractional free electromagnetic Lagrangian density using the radiation (Coulomb) gauge and Lorentz gauge. We also obtained fractional Euler-Lagrange (E-L) equations resulting from these Lagrangian densities. Then we found fractional Hamiltonian density in general form and used Dirac algebraic method to determine the creation and annihilation operators to construct the Canonical Commutation Relations (CCRs).

Keywords: Canonical quantization; Coulomb gauge; Lorentz gauge; Fractional derivative; Free electromagnetic lagrangian density.

Introduction

The theory of derivatives of non integer order goes back to Leibniz, Liouville, Riemann and Letnikov [1-9]. Fractional calculus generalizes the classical calculus and has many applications in various fields of physics. These applications include classical and quantum mechanics, field theory and electromagnetic theory formulated mostly in terms of left Riemann-Liouville fractional derivative [10-15].

The fractional variational principle represents an important part of fractional calculus and is deeply related to the fractional quantization procedure by obtaining the fractional Euler-Lagrange equation and the corresponding fractional Hamiltonian. The quantization of systems with fractional derivatives is an important area in the applications of fractional differential and integral calculus.

Canonical quantization is the procedure by which a classical theory, formulated by using the Lagrangian-Hamilton formalism, can be made into a quantum theory. The process of quantizing the Hamiltonian starts

with changing the coordinates and the conjugate momentum into operators, those satisfying commutation relations which correspond to the Poisson bracket relation of classical theory [16].

In the usual approach to the quantization of the free electromagnetic field, the gauge of the electromagnetic potentials is first fixed in either the radiation (Coulomb) gauge or the Lorentz gauge. If the radiation gauge is used, then a Fourier expansion of the transverse vector potential is made. When the Hamiltonian is expressed in terms of the vector potential, it reduces to a sum of uncoupled harmonic oscillator Hamiltonians. The harmonic oscillators are then canonically quantized. If the Lorentz gauge is used for quantization, subsidiary conditions must be imposed and an indefinite metric used to avoid contradictions. It must then be shown that the two procedures yield the same results, so that gauge invariance is ensured [17-19].

The main aim of this paper is to quantize the electromagnetic Lagrangian density with

Radiation and Lorentz gauge using left Riemann-Liouville fractional derivative and to obtain the fractional canonical commutation relations and compare them with the standard CCRs in classical calculus.

The plan of this paper is as follows: in the following section Riemann-Liouville fractional derivatives are briefly reviewed. Then, the fractional electromagnetic Lagrangian density and the canonical quantization in radiation gauge are dealt with. Then, the electromagnetic Lagrangian density and its canonical quantization in Lorentz gauge are presented. An appendix is inserted to show that the electromagnetic Lagrangian density is invariant under gauge transformation. Finally some concluding remarks are given.

Basic Definitions

Several definitions of a fractional derivative have been proposed. These definitions include Riemann-Liouville, Caputo, Marchaud and Riesz fractional derivatives [4-5]. In the following part of the paper, we briefly present some fundamental definitions used in this work. The left and right Riemann-Liouville fractional derivatives are defined as follows:

The left Riemann-Liouville fractional derivative

$${}_a D_t^\alpha f(t) = \left. \begin{aligned} & \frac{1}{\Gamma(n-\alpha)} \left(\frac{d}{dt} \right)^n \int_a^t (t-\tau)^{n-\alpha-1} f(\tau) d\tau \end{aligned} \right\} \quad (1)$$

The right Riemann-Liouville fractional derivative

$${}_t D_b^\alpha f(t) = \left. \begin{aligned} & \frac{1}{\Gamma(n-\alpha)} \left(-\frac{d}{dt} \right)^n \int_t^b (\tau-t)^{n-\alpha-1} f(\tau) d\tau \end{aligned} \right\} \quad (2)$$

where α represents the order of the derivative such that $n-1 \leq \alpha < n$ and Γ represents the Euler's gamma function. If α is an integer, these derivatives are defined in the usual sense; i.e.,

$${}_a D_t^\alpha f(t) = \left(\frac{d}{dt} \right)^\alpha$$

$${}_t D_b^\alpha f(t) = \left(-\frac{d}{dt} \right)^\alpha \quad \alpha = 1, 2, \dots$$

Riemann-Liouville fractional derivatives have many properties. One of these properties is that the R-L derivative of a constant is not zero, namely:

$${}_a D_t^\alpha A = A \frac{(t-a)^{-\alpha}}{\Gamma(1-\alpha)} \quad (3)$$

Another property is that the R-L derivative of a power t has the following form:

$${}_a D_t^\alpha t^\eta = \frac{\Gamma(\alpha+1)}{\Gamma(\eta-\alpha+1)} t^{\eta-\alpha} \quad (4)$$

$$\alpha > -1, \eta \geq 0$$

Finally, the fractional product rule is given below:

$${}_a D_t^\alpha (f g) = \sum_{j=0}^{\infty} \binom{\alpha}{j} {}_a D_t^{\alpha-j} f \frac{d^j g}{d t^j} \quad (5)$$

Fractional Canonical Quantization in Radiation (Coulomb) Gauge

Canonical quantization procedure amounts to the imposition of canonical commutation relations for the field variables and their canonically conjugate momenta. To quantize the free EM Lagrangian density in radiation (Coulomb) gauge, we will start to reformulate this Lagrangian density in fractional form using LRLFD procedure.

$$\mathcal{L} = \left[\begin{aligned} & \frac{1}{2} ({}_a D_{x_j}^\alpha \phi) ({}_a D_{x_j}^\alpha \phi) \\ & + \frac{1}{2} ({}_a D_t^\alpha A^j) ({}_a D_t^\alpha A^j) \\ & - \frac{1}{2} B^2 + ({}_a D_{x_j}^\alpha \phi) ({}_a D_t^\alpha A^j) \end{aligned} \right] \quad (6)$$

where

$$B^2 = {}_a D_{x_j}^\alpha A^k \left({}_a D_{x_j}^\alpha A^k - {}_a D_{x_k}^\alpha A^j \right)$$

${}_a D_{x^i}^\alpha \phi$, ${}_a D_{x^i}^\alpha A^i$ are the fractional gradient of scalar potential and vector potential, respectively.

Using radiation (Coulomb) gauge ${}_a D_{x^i}^\alpha A^i = 0$, $\varphi = 0$, we get

$$\mathcal{L} = \frac{1}{2} \left({}_a D_t^\alpha A^j \right) \left({}_a D_t^\alpha A^j \right) - \frac{1}{2} \left({}_a D_{x^j}^\alpha A^i \right) \left({}_a D_{x^j}^\alpha A^i \right) \quad (7)$$

From this definition of Lagrangian density, we obtain the fractional (E-L) equation by applying the general formula given by Agrawal [8] as:

$$\frac{\partial \mathcal{L}}{\partial \varphi_\rho} + \left[\begin{array}{l} {}_a D_{x^\mu}^\alpha \left(\frac{\partial \mathcal{L}}{\partial {}_a D_{x^\mu}^\beta \varphi_\rho} \right) \\ + {}_a D_{x^\mu}^\beta \left(\frac{\partial \mathcal{L}}{\partial {}_a D_{x^\mu}^\alpha \varphi_\rho} \right) \end{array} \right] = 0 \quad (8)$$

For field variables A^i, A^j we get the equation:

$$0 = -{}_a D_t^\alpha \left\{ -{}_a D_{x^j}^\alpha \phi - {}_a D_t^\alpha A^j \right\} + {}_a D_{x^j}^\alpha \left\{ {}_a D_{x^j}^\alpha A^i - {}_a D_{x^j}^\alpha A^i \right\} \quad (9)$$

Since $\varphi=0$, we get

$$-{}_a D_t^\alpha \left\{ -{}_a D_t^\alpha A^j \right\} + {}_a D_{x^j}^\alpha \left\{ {}_a D_{x^j}^\alpha A^i - {}_a D_{x^j}^\alpha A^i \right\} = 0 \quad (10)$$

Equation (9) represents the second non-homogeneous Maxwell's equation in fractional form, where $(-{}_a D_{x^j}^\alpha \phi - {}_a D_t^\alpha A^j)$ and $({}_a D_{x^j}^\alpha A^i - {}_a D_{x^j}^\alpha A^i)$ are the fractional electric and magnetic fields, respectively.

Equation (10) can be represented as wave equation:

$$\left({}_a D_{x^j}^\alpha {}_a D_{x^j}^\alpha - {}_a D_t^\alpha {}_a D_t^\alpha \right) A^j = 0 \quad (11)$$

where A^j is the vector potential which takes the plane wave solution.

Then

$$A^i(t, x) = \sum_{\lambda=1,2} \int \frac{d^3 k}{(2\pi)^3 \sqrt{2\omega_k}} \left\{ \begin{array}{l} a_k^i \varepsilon_\lambda^i e^{-ik \cdot x} \\ + a_k^{+i} \varepsilon_\lambda^i e^{ik \cdot x} \end{array} \right\} \quad (12)$$

where ε_λ^i is the polarization vector which has the following properties:

$$k^i \varepsilon_\lambda^i = 0 \quad (13)$$

$$\varepsilon_\lambda^i \varepsilon_{\lambda'}^i = \delta_{\lambda\lambda'} \quad (14)$$

Here $\lambda = 1, 2$ is the polarization state and a_λ^i , a_λ^{+i} are the creation and annihilation operators.

To start the quantization process of the free EM Lagrangian density, we have to introduce the Hamiltonian density in fractional form using LRLFD as:

$$\mathcal{H} = \pi^i {}_a D_t^\alpha A^i + \pi^j {}_a D_t^\alpha A^j - \mathcal{L} \quad (15)$$

$$\text{But, } \pi^i = 0, \pi^j = \frac{\partial \mathcal{L}}{\partial {}_a D_t^\alpha A^j} = {}_a D_t^\alpha A^j$$

Then

$$\mathcal{H} = \frac{1}{2} \left[\left({}_a D_t^\alpha A^j \right)^2 + \left({}_a D_{x^j}^\alpha A^i \right)^2 \right] \quad (16)$$

Using the definition $\pi^j = {}_a D_t^\alpha A^j$, we get:

$$\mathcal{H} = \frac{1}{2} \left[\left(\pi^j \right)^2 + \left({}_a D_{x^j}^\alpha A^i \right)^2 \right] \quad (17)$$

We can generalize this formulation in fractional form in terms of η, γ as:

$$\mathcal{H}_{\eta,\gamma} = \frac{1}{2} \left[\left({}_a D_{x^j}^\alpha A^i \right)^\eta + \left(\pi^j \right)^\gamma \right] \quad (18)$$

where η, γ noninteger numbers.

Using algebraic method in quantum mechanics:

$$\mathcal{H}_{\eta,\gamma} = \frac{1}{\sqrt{2}} \left[\left({}_a D_{x^j}^\alpha A^i \right)^\frac{\eta}{2} + i \left(\pi^j \right)^\frac{\gamma}{2} \right] \times \left\{ \begin{array}{l} \\ \frac{1}{\sqrt{2}} \left[\left({}_a D_{x^j}^\alpha A^i \right)^\frac{\eta}{2} - i \left(\pi^j \right)^\frac{\gamma}{2} \right] \end{array} \right\} \quad (19)$$

where

$$a_k^i \varepsilon_\lambda^i = \frac{1}{\sqrt{2}} \left[({}_a D_{x^j} A^i)^{\frac{\eta}{2}} + i(\pi^j)^{\frac{\gamma}{2}} \right] \quad (20)$$

$$a_k^{+i} \varepsilon_\lambda^{+i} = \frac{1}{\sqrt{2}} \left[({}_a D_{x^j} A^i)^{\frac{\eta}{2}} - i(\pi^j)^{\frac{\gamma}{2}} \right] \quad (21)$$

We construct the canonical commutation relations CCRs in fractional form:

$$\left. \begin{aligned} [a_k^i \varepsilon_\lambda^i, a_k^{+i} \varepsilon_\lambda^{+i}] = \\ \varepsilon_\lambda^i \varepsilon_\lambda^{+i} a_k^i a_k^{+i} - \varepsilon_\lambda^{+i} \varepsilon_\lambda^i a_k^{+i} a_k^i \end{aligned} \right\} \quad (22)$$

Using the definitions in equations (20) and (21), we obtain:

$$\left. \begin{aligned} \varepsilon_\lambda^i \varepsilon_\lambda^{+i} a_k^i a_k^{+i} = \\ \mathcal{H}_{\eta,\gamma} + \frac{i}{2} \left[(\pi^j)^{\frac{\gamma}{2}}, ({}_a D_{x^j} A^i)^{\frac{\eta}{2}} \right] \end{aligned} \right\} \quad (23)$$

$$\left. \begin{aligned} \varepsilon_\lambda^{+i} \varepsilon_\lambda^i a_k^{+i} a_k^i = \\ \mathcal{H}_{\eta,\gamma} - \frac{i}{2} \left[(\pi^j)^{\frac{\gamma}{2}}, ({}_a D_{x^j} A^i)^{\frac{\eta}{2}} \right] \end{aligned} \right\} \quad (24)$$

Substituting these results in equation (22), we get:

$$\left. \begin{aligned} [a_k^i \varepsilon_\lambda^i, a_k^{+i} \varepsilon_\lambda^{+i}] = \\ i \left[(\pi^j)^{\frac{\gamma}{2}}, ({}_a D_{x^j} A^i)^{\frac{\eta}{2}} \right] \end{aligned} \right\} \quad (25)$$

$$\left. \begin{aligned} [a_k^i \varepsilon_\lambda^i, a_k^{+i} \varepsilon_\lambda^{+i}] = \\ -i \left[({}_a D_{x^j} A^i)^{\frac{\eta}{2}}, (\pi^j)^{\frac{\gamma}{2}} \right] \end{aligned} \right\} \quad (26)$$

Since $(\pi^j)^{\frac{\gamma}{2}}$ is the canonical momentum conjugate to the $(A^i)^{\frac{\eta}{2}}$ coordinate, we can

write it as [3, 4] $(\pi^j)^{\frac{\gamma}{2}} = \left(\frac{\hbar}{i} \frac{\partial}{\partial A^{\frac{\eta}{2}}} \right)^{\frac{\gamma}{2}}$.

Then, the CCRs become like:

$$\left. \begin{aligned} [a_k^i \varepsilon_\lambda^i, a_k^{+i} \varepsilon_\lambda^{+i}] = \\ -i \left[({}_a D_{x^j} A^i)^{\frac{\eta}{2}}, \left(\frac{\hbar}{i} \frac{\partial}{\partial A^{\frac{\eta}{2}}} \right)^{\frac{\gamma}{2}} \right] \end{aligned} \right\} \quad (27)$$

Rearranging this equation, we get:

$$\left. \begin{aligned} [a_k^i \varepsilon_\lambda^i, a_k^{+i} \varepsilon_\lambda^{+i}] F = \\ -i ({}_a D_{x^j})^{\frac{\eta}{2}} \left(\frac{\hbar}{i} \right)^{\frac{\gamma}{2}} \left[(A^i)^{\frac{\eta}{2}}, \left(\frac{\partial}{\partial A^{\frac{\eta}{2}}} \right)^{\frac{\gamma}{2}} \right] F \end{aligned} \right\} \quad (28)$$

This means that

$$\left. \begin{aligned} [a_k^i \varepsilon_\lambda^i, a_k^{+i} \varepsilon_\lambda^{+i}] F = \\ -i \left(\frac{\hbar}{i} \right)^{\frac{\gamma}{2}} ({}_a D_{x^j})^{\frac{\eta}{2}} \left\{ \begin{aligned} & (A^i)^{\frac{\eta}{2}} \left(\frac{\partial}{\partial A^{\frac{\eta}{2}}} \right)^{\frac{\gamma}{2}} F \\ & - \left(\frac{\partial}{\partial A^{\frac{\eta}{2}}} \right)^{\frac{\gamma}{2}} \left[(A^i)^{\frac{\eta}{2}} F \right] \end{aligned} \right\} \end{aligned} \right\}$$

Using Leibniz rule to rewrite the second term in the square brackets, we obtain as in [ref. 20]:

$$\left. \begin{aligned} [a_k^i \varepsilon_\lambda^i, a_k^{+i} \varepsilon_\lambda^{+i}] F = -i \left(\frac{\hbar}{i} \right)^{\frac{\gamma}{2}} ({}_a D_{x^j})^{\frac{\eta}{2}} \left\{ \begin{aligned} & (A^i)^{\frac{\eta}{2}} \frac{\partial^{\frac{\gamma}{2}}}{\partial A^{\frac{\eta}{2}}} F - \sum_{r=0}^{\frac{\gamma}{2}} \binom{\frac{\gamma}{2}}{r} \frac{\partial^{\frac{\gamma}{2}-r}}{\partial A^{\frac{\eta}{2}}} (A^i)^{\frac{\eta}{2}} \frac{\partial^r}{\partial A^{\frac{\eta}{2}}} F \end{aligned} \right\} \end{aligned} \right\} \quad (29)$$

As a special case, taking $\eta = \gamma = 2$, the CCRs reduce to the original relations like

$$\left. \begin{aligned} [a_k^i \varepsilon_\lambda^i, a_k^{+i} \varepsilon_\lambda^{+i}] = \\ -i \nabla \frac{\hbar}{i} \left\{ A \frac{\partial F}{\partial A} - F \frac{\partial A}{\partial A} - A \frac{\partial F}{\partial A} \right\} \end{aligned} \right\}$$

$$\left[a_k^i \varepsilon_\lambda^i, a_k^{+i} \varepsilon_\lambda^{+i} \right] = \hbar \nabla F$$

Finally, let us write the Hamiltonian density in terms of creation and annihilation operators.

Since

$$\mathcal{H} = \frac{1}{2} \left[\left(\pi^j \right)^2 + \left({}_a D_{x^j}^\alpha A^i \right)^2 \right]$$

Using these definitions we get

$$\nabla^\beta A^i(t, x) = {}_a D_{x^\beta}^\alpha A^i = \sum_{\lambda=1,2} \int \frac{d^3 k}{(2\pi)^3 \sqrt{2\omega_k}} \left\{ -ik \right\}^\beta \left\{ \begin{array}{l} a_k^i \varepsilon_\lambda^i e^{-ik \cdot x} \\ + (-1)^\beta a_k^{+i} \varepsilon_\lambda^{+i} e^{ik \cdot x} \end{array} \right\}$$

Then

$$\mathcal{H}_{\eta, \gamma} = \frac{1}{2} \left[\varepsilon_\lambda^i \varepsilon_\lambda^{+i} a_k^i a_k^{+i} + \varepsilon_\lambda^{+i} \varepsilon_\lambda^i a_k^{+i} a_k^i \right] \quad (30)$$

Also, we can obtain other CCRs like:

$$\left[a_k^i \varepsilon_\lambda^i, \mathcal{H} \right] = \varepsilon_\lambda^i \varepsilon_\lambda^{+i} a \left[a_k^i \varepsilon_\lambda^i, a_k^{+i} \varepsilon_\lambda^{+i} \right]$$

$$\left[a_k^{+i} \varepsilon_\lambda^{+i}, \mathcal{H} \right] = \varepsilon_\lambda^{+i} \varepsilon_\lambda^i a \left[a_k^{+i} \varepsilon_\lambda^{+i}, a_k^i \varepsilon_\lambda^i \right]$$

$$\left[a_k^i \varepsilon_\lambda^i, a_k^j \varepsilon_\lambda^j \right] = \left[a_k^{+i} \varepsilon_\lambda^{+i}, a_k^{+j} \varepsilon_\lambda^{+j} \right] = 0$$

Fractional Canonical Quantization in Lorentz Gauge

As in the previous section, let us rewrite the electromagnetic Lagrangian density in Lorentz gauge ${}_a D_{x^\mu}^\alpha A^\mu = 0$. Here, we need a term containing the time derivative of ϕ in order to insure the existence of the canonically conjugate field π° . Fermi added this term to the electromagnetic Lagrangian density, so the electromagnetic Lagrangian density can be written in fractional form using LRLFD as:

$$\mathcal{L} = \frac{-1}{2} \left[\begin{array}{l} {}_a D_t^\alpha A_j {}_a D_t^\alpha A^j - {}_a D_t^\alpha A_j {}_a D_{x^j}^\alpha \phi \\ + {}_a D_{x^i}^\alpha \phi {}_a D_{x^i}^\alpha \phi - {}_a D_{x^i}^\alpha \phi {}_a D_t^\alpha A^i \\ + {}_a D_{x^i}^\alpha A_j {}_a D_{x^i}^\alpha A^j \\ - {}_a D_{x^i}^\alpha A_j {}_a D_{x^j}^\alpha A^i \end{array} \right] - \frac{1}{2} \xi \left[{}_a D_t^\alpha \phi {}_a D_t^\alpha \phi + {}_a D_{x^l}^\alpha A^l {}_a D_{x^l}^\alpha A^l \right] \quad (31)$$

$$A^i(t, x) = \sum_{\lambda=1,2} \int \frac{d^3 k}{(2\pi)^3 \sqrt{2\omega_k}} \left\{ \begin{array}{l} a_k^i \varepsilon_\lambda^i e^{-ik \cdot x} \\ + a_k^{+i} \varepsilon_\lambda^{+i} e^{ik \cdot x} \end{array} \right\}$$

$$\pi^j(t, x) = \sum_{\lambda=1,2} \int \frac{d^3 k}{(2\pi)^3 \sqrt{2\omega_k}} \left\{ i\omega_k \right\} \left\{ \begin{array}{l} a_k^i \varepsilon_\lambda^i e^{-ik \cdot x} \\ - a_k^{+i} \varepsilon_\lambda^{+i} e^{ik \cdot x} \end{array} \right\}$$

where ξ is a freely chosen parameter.

The Euler- Lagrange equation for this Lagrangian formulation can be obtained using equation (8).

For field variable ϕ , (E-L) equation takes the form:

$$\xi {}_a D_t^\alpha {}_a D_t^\alpha \phi + {}_a D_{x^i}^\alpha \left(-{}_a D_{x^i}^\alpha \phi - {}_a D_t^\alpha A^j \right) = 0 \quad (32)$$

This is similar to the first non-homogeneous Maxwell's equation in free field except that there is an additional term coming from the added term to the EM Lagrangian density.

Now, for the fields A^i, A^j , we obtain the other equation by the same method. Then we get:

$$\left. \begin{array}{l} -{}_a D_t^\alpha \left(-{}_a D_{x^i}^\alpha \phi - {}_a D_t^\alpha A^j \right) \\ + {}_a D_{x^j}^\alpha \left\{ {}_a D_{x^i}^\alpha A_j - {}_a D_{x^j}^\alpha A_i \right\} \\ + \xi {}_a D_{x^l}^\alpha {}_a D_{x^l}^\alpha A^l \\ = 0 \end{array} \right\} \quad (33)$$

This equation is similar to the second Maxwell's equation in free field, and the only difference is the added term coming from the added term to the Lagrangian density.

After the preparations given above, the stage now is set for fractional quantization of this Lagrangian density.

Using Feynmann gauge $\xi=1$, the EM Lagrangian density takes the form:

$$\mathcal{L} = -\frac{1}{2} {}_a D_{x^\mu}^\alpha A_\nu {}_a D_{x^\mu}^\alpha A^\nu \quad (34)$$

Now, using the definition of the Hamiltonian

$$\mathcal{H} = \pi^\mu {}_a D_t^\alpha A^\mu - \mathcal{L}$$

we obtain

$$\mathcal{H} = -\frac{1}{2} \left\{ \pi_\mu \pi^\mu + {}_a D_{x^i}^\alpha A^\nu {}_a D_{x^i}^\alpha A^\nu \right\} \quad (35)$$

This formulation can be generalized in fractional form as:

$$\mathcal{H}_{\gamma,\eta} = \frac{-1}{2} \left\{ (\pi_\mu)^\gamma + ({}_a D_{x^i}^\alpha A^\nu)^\eta \right\} \quad (36)$$

$$\mathcal{H}_{\gamma,\eta} = \frac{i^2}{2} \left\{ ({}_a D_{x^i}^\alpha A^\nu)^\eta + (\pi_\mu)^\gamma \right\} \quad (37)$$

Using the algebraic method in quantum mechanics, we get:

$$\mathcal{H}_{\gamma,\eta} = \frac{i}{\sqrt{2}} \left\{ ({}_a D_{x^i}^\alpha A^\nu)^\eta + i(\pi_\mu)^\gamma \right\} \times \left. \begin{array}{l} \\ \\ \frac{i}{\sqrt{2}} \left\{ ({}_a D_{x^i}^\alpha A^\nu)^\eta - i(\pi_\mu)^\gamma \right\} \end{array} \right\} \quad (38)$$

Let $\varepsilon_\lambda^i a_k^i$, $\varepsilon_\lambda^{+i} a_k^{+i}$ be the creation and annihilation operators:

$$\varepsilon_\lambda^i a_k^i = \frac{i}{\sqrt{2}} \left[{}_a D_{x_j}^{\frac{\eta}{2}} (A_\nu)^\frac{\eta}{2} + i(\pi_\mu)^\frac{\gamma}{2} \right] \quad (39)$$

$$\varepsilon_\lambda^{+i} a_k^{+i} = \frac{i}{\sqrt{2}} \left[{}_a D_{x_j}^{\frac{\eta}{2}} (A_\nu)^\frac{\eta}{2} - i(\pi_\mu)^\frac{\gamma}{2} \right] \quad (40)$$

$$\left[\varepsilon_\lambda^i a_k^i, \varepsilon_\lambda^{+i} a_k^{+i} \right] F = i \left(\frac{\hbar}{i} \right)^\frac{\gamma}{2} {}_a D_{x_j}^{\frac{\eta}{2}} \left\{ (A_\nu)^\frac{\eta}{2} \left(\frac{\partial}{\partial (A_\nu)^\frac{\eta}{2}} \right)^\frac{\gamma}{2} F - \sum_{r=0}^{\frac{\gamma}{2}} \left(\frac{\alpha}{2} \right) \binom{\frac{\gamma}{2}}{r} \left(\frac{\partial}{\partial (A_\nu)^\frac{\eta}{2}} \right)^\frac{\gamma}{2-r} (A_\nu)^\frac{\eta}{2} \frac{\partial^r F}{\partial^r (A_\nu)^\frac{\eta}{2}} \right\} \quad (45)$$

Now construct the canonical commutation relations as:

$$\left[\varepsilon_\lambda^i a_k^i, \varepsilon_\lambda^{+i} a_k^{+i} \right] = \varepsilon_\lambda^i \varepsilon_\lambda^{+i} a_k^i a_k^{+i} - \varepsilon_\lambda^{+i} \varepsilon_\lambda^i a_k^{+i} a_k^i$$

Using the same procedure as in the previous section, we get:

$$\left[\varepsilon_\lambda^i a_k^i, \varepsilon_\lambda^{+i} a_k^{+i} \right] = i \left[{}_a D_{x_j}^{\frac{\eta}{2}} (A_\nu)^\frac{\eta}{2}, (\pi_\mu)^\frac{\gamma}{2} \right] \quad (41)$$

$$\left[\varepsilon_\lambda^i a_k^i, \varepsilon_\lambda^{+i} a_k^{+i} \right] = i {}_a D_{x_j}^{\frac{\eta}{2}} \left[(A_\nu)^\frac{\eta}{2}, (\pi_\mu)^\frac{\gamma}{2} \right] \quad (42)$$

Since $(\pi^j)^\frac{\gamma}{2}$ is the canonical conjugate to the $(A^j)^\frac{\eta}{2}$, we can write:

$$\left(\pi^j \right)^\frac{\gamma}{2} = \left(\frac{\hbar}{i} \frac{\partial}{\partial (A^j)^\frac{\eta}{2}} \right)^\frac{\gamma}{2} \left. \begin{array}{l} \left[\varepsilon_\lambda^i a_k^i, \varepsilon_\lambda^{+i} a_k^{+i} \right] = \\ i {}_a D_{x_j}^{\frac{\eta}{2}} \left[(A_\nu)^\frac{\eta}{2}, \left(\frac{\hbar}{i} \frac{\partial}{\partial (A_\nu)^\frac{\eta}{2}} \right)^\frac{\gamma}{2} \right] \end{array} \right\} \quad (43)$$

Rearranging this equation, we get:

$$\left[\varepsilon_\lambda^i a_k^i, \varepsilon_\lambda^{+i} a_k^{+i} \right] F = i \left(\frac{\hbar}{i} \right)^\frac{\gamma}{2} {}_a D_{x_j}^{\frac{\eta}{2}} \left[(A_\nu)^\frac{\eta}{2}, \left(\frac{\partial}{\partial (A_\nu)^\frac{\eta}{2}} \right)^\frac{\gamma}{2} \right] F \quad (44)$$

Using Leibniz rule, we obtain this equation as in [20]

As a special case $\eta = \gamma = 2$, then

$$\left[\varepsilon_{\lambda}^i a_k^i, \varepsilon_{\lambda}^{+i} a_k^{+i} \right] F = -\hbar \nabla F$$

Finally, to obtain the Hamiltonian density in terms of creation and annihilation operators, we start with the definition of A^{μ} , π_{μ} , where the vector potential A^{μ} can be expanded into plane waves as:

$$A^{\mu}(t, x) = \left. \int \frac{d^3 k}{\sqrt{(2\pi)^3 2\omega_k}} \sum_{\lambda=0}^3 \left[a_{\lambda}^{\mu}(k) \varepsilon_{\lambda}^{\mu} e^{-ik \cdot x} + a_{\lambda}^{+\mu}(k) \varepsilon_{\lambda}^{+\mu} e^{ik \cdot x} \right] \right\} \quad (46)$$

The canonically conjugate variable takes the form:

$$\pi^{\mu}(t, x) = \left. i \int \frac{d^3 k}{\sqrt{(2\pi)^3 2\omega_k}} \sum_{\lambda=0}^3 \left[a_{\lambda}^{\mu}(k) \varepsilon_{\lambda}^{\mu} e^{-ik \cdot x} - a_{\lambda}^{+\mu}(k) \varepsilon_{\lambda}^{+\mu} e^{ik \cdot x} \right] \right\} \quad (47)$$

where $\omega_k = k_0 = |k|$, $\lambda = 0, 1, 2, 3$ (polarization state), $\varepsilon_{\lambda}^{\mu}$ is a set of 4 linearly independent vectors which may assume real.

Then we get:

$$\mathcal{H} = \sum_{\lambda=0}^3 -g_{\lambda\lambda} a_{k\lambda}^+ a_{k\lambda} \quad (48)$$

where $g_{\lambda\lambda} = 1, -1, -1, -1$

We also found other commutation relations like:

$$\begin{aligned} \left[\varepsilon_{\lambda}^i a_k^i, \mathcal{H} \right] &= \varepsilon_{\lambda}^i a_k^i \left[\varepsilon_{\lambda}^i a_k^i, \varepsilon_{\lambda}^{+i} a_k^{+i} \right] \\ \left[\varepsilon_{\lambda}^{+i} a_k^{+i}, \mathcal{H} \right] &= \varepsilon_{\lambda}^{+i} a_k^{+i} \left[\varepsilon_{\lambda}^{+i} a_k^{+i}, \varepsilon_{\lambda}^i a_k^i \right] \\ \left[\varepsilon_{\lambda}^i a_k^i, \varepsilon_{\lambda}^j a_k^j \right] &= \left[\varepsilon_{\lambda}^{+i} a_k^{+i}, \varepsilon_{\lambda}^{+j} a_k^{+j} \right] = 0 \end{aligned}$$

Appendix

Gauge Invariance of Lagrangian Density

The Lagrangian density for the fractional electromagnetic field \mathcal{L} is given by equation (6). Variation of \mathcal{L} with respect to the fractional potential A_{μ} yields the fractional inhomogeneous Maxwell's equations.

The potential A_{μ} is not uniquely determined. A change of the potential of the type $A'_{\mu} = A_{\mu} + \partial_{\mu} \Lambda$ leaves the electromagnetic field unchanged and therefore is called a gauge invariant $\mathcal{L}' \rightarrow \mathcal{L}$ [21].

We can rewrite equation (6) using the definition of the vector potential in 4 dimensions as:

$$A^{\mu} = \phi, A^j, \partial_{\mu} = {}_a D_{x_{\mu}}^{\alpha} = {}_a D_t^{\alpha}, {}_a D_{x_j}^{\alpha}, \Lambda$$

scalar function

$$\mathcal{L} = \frac{-1}{2} \begin{bmatrix} {}_a D_{x_{\mu}}^{\alpha} A_{\nu} & {}_a D_{x_{\mu}}^{\alpha} A^{\nu} \\ -{}_a D_{x_{\mu}}^{\alpha} A_{\nu} & {}_a D_{x_{\nu}}^{\alpha} A'^{\mu} \end{bmatrix} \quad (A-1)$$

$$\mathcal{L}' = \frac{-1}{2} \begin{bmatrix} {}_a D_{x_{\mu}}^{\alpha} A'_{\nu} & {}_a D_{x_{\mu}}^{\alpha} A'^{\nu} \\ -{}_a D_{x_{\mu}}^{\alpha} A'_{\nu} & {}_a D_{x_{\nu}}^{\alpha} A'^{\mu} \end{bmatrix} \quad (A-2)$$

where $A'^{\nu} = A^{\nu} + \partial^{\nu} \Lambda$, $A'^{\mu} = A^{\mu} + \partial^{\mu} \Lambda$

μ, ν, λ space-time dimension

i, j, k space dimension

$$\mathcal{L}' = \frac{-1}{2} \begin{bmatrix} {}_a D_{x_{\mu}}^{\alpha} (A_{\nu} + \partial_{\nu} \Lambda) \times \\ {}_a D_{x_{\mu}}^{\alpha} (A^{\nu} + \partial^{\nu} \Lambda) \\ -{}_a D_{x_{\mu}}^{\alpha} (A_{\nu} + \partial_{\nu} \Lambda)_{\nu} \times \\ {}_a D_{x_{\nu}}^{\alpha} (A^{\mu} + \partial^{\mu} \Lambda) \end{bmatrix}$$

Then

$$\mathcal{L}' = \frac{-1}{2} \left[\begin{array}{l} \left({}_a D_{x_\mu}^\alpha A_\nu \quad {}_a D_{x^\mu}^\alpha A^\nu \right) \\ + \left({}_a D_{x_\mu}^\alpha A_\nu \quad {}_a D_{x^\mu}^\alpha \partial^\nu \Lambda \right) \\ + \left({}_a D_{x_\mu}^\alpha \partial_\nu \Lambda \quad {}_a D_{x^\mu}^\alpha A^\nu \right) \\ + \left({}_a D_{x_\mu}^\alpha \partial_\nu \Lambda \quad {}_a D_{x^\mu}^\alpha \partial^\nu \Lambda \right) \\ - \left({}_a D_{x_\mu}^\alpha A_\nu \quad {}_a D_{x^\nu}^\alpha A^\mu \right) \\ - \left({}_a D_{x_\mu}^\alpha A_\nu \quad {}_a D_{x^\nu}^\alpha \partial^\mu \Lambda \right) \\ - \left({}_a D_{x_\mu}^\alpha \partial_\nu \Lambda \quad {}_a D_{x^\nu}^\alpha A^\mu \right) \\ - \left({}_a D_{x_\mu}^\alpha \partial_\nu \Lambda \quad {}_a D_{x^\nu}^\alpha \partial^\mu \Lambda \right) \end{array} \right] \quad (\text{A-3})$$

which can be simplified into

$$\mathcal{L}' = \frac{-1}{2} \left[\begin{array}{l} {}_a D_{x_\mu}^\alpha A_\nu \quad {}_a D_{x^\mu}^\alpha A^\nu \\ - {}_a D_{x_\mu}^\alpha A_\nu \quad {}_a D_{x^\nu}^\alpha A^\mu \end{array} \right] \quad (\text{A-4})$$

So $\mathcal{L}' = \mathcal{L}$

That is the Lagrangian density. It is invariant under gauge transformation, which is the current (charge) is conserved.

Conclusion

The fractional quantization of field theory is not an easy task, especially when the fractional Hamiltonian is complicated. Here, we have quantized the free EM Lagrangian density in both radiation (Coulomb) gauge and Lorentz gauge. For the two cases, we obtained the Hamiltonian in terms of vector potential and also in terms of creation and annihilation operators, then we constructed the fractional canonical commutation relations. We have shown that the two gauges yield the same results, since the Hamiltonian reduces into a sum of uncoupled harmonic oscillator Hamiltonians for two cases.

References

- [1] Baleanu, D., Golmankhaneh, A.K. and Baleanu, M., *Int. J. Theor. Phys.* 48 (2009) 3114.
- [2] Muslih, S.I., Agrawal, O.P. and Baleanu, D., *Int. J. Theor. Phys.* (2010) DOI 10.1007/s10773-010-0354-x.
- [3] Muslih, S.I., *Int. J. Theor. Phys.* (2010) DOI 10.1007/s10773-010-0396-0.
- [4] Podlubny, I., *Fractional Differential Equations*, (Academic Press, NewYork, 1999).
- [5] Oldham, K.B. and Spanier, J., *The Fractional Calculus*, (Academic Press, New York, 1974).
- [6] Riewe, F., *Phys. Rev. E*, 53 (1996) 1890.
- [7] Riewe, F., *Phys. Rev. E*, 55 (1997) 3582.
- [8] Agrawal, O.P., *J. Math. Anal. Appl.* 272 (2002) 368.
- [9] Baleanu, D. and Muslih, S.I., *Czech. J. Phys.* 55(6) (2005) 633.
- [10] Hilfer, R., *Applications of Fraction Calculus in Physics*, (World Scientific Publishing Company, Singapore, NewJersy, London and Hong Kong, 2000).
- [11] Baleanu, D. and Muslih, S.I., *Czech. J. Phys.* 55(9) (2005) 1063.
- [12] Agrawal, O.P., *Nonlinear Dynamics*, 38 (2004) 191.
- [13] Agrawal, O.P., *Nonlinear Dynamics*, 38 (2004) 323.
- [14] Muslih, S.I. and Baleanu, D., *Nuovo Cimento*, 120 (2005) 507.
- [15] Dirac, P.A.M., (Yeshiva University, New York, 1964).
- [16] Gray, R.D. and Kobe, D.H., *J. Phys. A: Math. Gen.* 15 (1982) 3145.
- [17] Laskin, N., *Phys. Lett. A*, 268 (2000) 298.
- [18] Laskin, N., *Phys. Rev. E*, 66 (2002) 056108.
- [19] Jaradat, E.K., Ph.D. Thesis, University of Jordan (2009).
- [20] Erikson, E. and Leinass, J.M., *Physica Scripta*, 22 (1980) 199.
- [21] Jackson J.D., *Classical Electrodynamics*, JohnWiley, second edition (1980).

Comparative Study of the Conductivity Percolation Behaviour of Nanocomposite Thin Layers Made of Nanoparticulate ITO and Carbon Nanotubes Colloids

Naji Al Dahoudi

Physics Department, Al-Azhar University, P.O. Box 1277, Gaza, Palestine.

Received on: 7/3/2010; Accepted on: 29/6/2010

Abstract: The electrical conductivity behaviour of two transparent conducting nanocomposite thin films made of nanoparticulate indium tin oxide (ITO) and carbon multiwall nanotubes (MWNTs) colloids deposited on a polycarbonate substrate was studied. The carbon MWNTs films exhibit a low critical threshold (0.083 vol. %) compared with that of the ITO films (0.19 vol. %). The surface morphology of the films shows stronger aggregation of the carbon MWNTs above the critical threshold. The electrical conductivity obtained for the ITO films is 526 Sm^{-1} , which is larger than that obtained for the carbon MWNTs films (65 Sm^{-1}). The optical properties of ITO films show higher transmission in the visible range with a smaller transmission window than that of the carbon MWNTs. Both coatings show similar mechanical properties against abrasion with a very good adhesion on the plastic substrate.

Keywords: Colloid; Electrical conductivity; Thin films; ITO nanoparticles; Carbon nanotubes.

PACS: 81.20.FW

Introduction

The electric conducting percolation behaviour in nanocomposite systems composed of mixtures of conducting and insulating species have gained an increasing interest due to their applications in thin film technology, e.g. for electromagnetic shielding, antistatic purposes and corrosion protection [1-5]. The electrical properties of such systems depend on the dispersion of the conducting fillers, their size and aggregate structure formed in the host insulating matrix [6-8]. These systems have poor electrical conductivity below a certain volume fraction of the conducting filler defined as the critical threshold, where there are no contacts between adjacent filler particles. Above the critical threshold, agglomerates are grown to reach a size which makes it possible for them to touch each other resulting in a formation of a conductive network within the insulating

phase. To understand the network formation, there are many so-called percolation models. A review on various models was given by Lux [9] and Clerc *et al.* [10].

Coating plastic substrates of functional layers is the aim of many researchers. In most applications, the layers must possess a combination of mechanical, electrical and optical properties as well. For example, low electrical conductivity ($\sim 10^{-4} \text{ Sm}^{-1}$) to dissipate static charge build up is necessary besides high electrical transparency and good mechanical durability. However, because of their poor thermal stability, the deposition techniques available to coat such substrates are therefore limited. So, the route to get transparent conductive coatings on plastics is to use composites that can be fully treated at relatively low temperatures ($T < 200 \text{ }^\circ\text{C}$). The most used materials are conductive fillers

dispersed in an inorganic-organic matrix. Among the most important conducting materials, there are n-type oxide semiconductors (TCO) such as indium tin oxide (ITO) and fluorine or antimony doped tin dioxide (FTO, ATO) [8]. $\text{In}_2\text{O}_3:\text{Sn}$ (ITO) has attracted the highest attention for its high conductivity though the relatively high price often limits its use. Conjugated polymers, such as polyaniline and polypyrrole, are among the best conducting polymers which are widely used as transparent conducting films [11, 12]. Carbon nanotubes are very interesting materials which drive remarkable scientific researches including chemistry, electronic transport, mechanical and field emission properties. The use of carbon nanotubes to impart electrical conductivity while maintaining high optical transparency is nowadays possible [13-15]. They have potential applications as catalyst supports, as cathodes in field emission displays and as electrodes [16]. The unique quality of this form of carbon is simple in that the individual particles possess the attributes of high electrical conductivity and high aspect ratio combined with a unique capability of forming ropes of individual particles. The combination of all these properties allows the formation of conductive networks through the materials with tunable electrical resistivity and good transparency.

In this work, a comparative study between tin doped indium oxide (ITO) nanoparticles and carbon multiwall nanotubes as conductive fillers dispersed in an inorganic-organic matrix and deposited on a plastic substrate at low temperature was conducted. The optical and mechanical properties of both systems are also given.

Experimental

Two coating sols were prepared to be deposited onto a polycarbonate (PC) substrate. The first one is alcoholic colloid based on crystalline ITO nanoparticles having an average crystallite size of 25 nm (cubic In_2O_3 cubic structure). ITO paste of 75 vol. % solid content was added to a Glycidoxypropyltrimethoxysilane (GPTS) under hydrolysis. The obtained sol was diluted with 1-Propanol in an ultrasonic bath. The loading ratio of ITO nanoparticles to the

GPTS matrix was adjusted between 0.05 and 0.9 vol. %.

The second coating sol was an aqueous suspension containing carbon MWNTs from Nanocyl S.A as conducting filler with a solid content up to 10 mg / ml. The suspension was dispersed using a dispersion agent called hexadecyl trimethyl ammonium chloride (HDTAC, Fluka, 98%) in doubly distilled water by mixing them under stirring in an ultrasonic bath, then supplied to a microfluidizer and pumped under 1700 bar pressure for 10 min. The obtained suspension was then added to the GPTS under hydrolysis to provide a range of carbon MWNTs loading from 0.05 to 0.6 volume fraction.

Both sols were filtered and then deposited on 3 mm thick PC substrates using the spin coating techniques with a spinning speed of 2000 rpm. The wet layers were dried for 10 min at 40 °C and then heated in an oven for 30 min at a temperature of 130°C.

The electrical properties of the films were characterized by measuring the sheet resistance (R) using a contactless non-destructive system from Leighton Electronics, Inc. The electrical resistivity (ρ) of the films was determined by $\rho = R \times t$, where t is the thickness of the films, measured with a Tencor P-10 surface profilometer. The electrical conductivity (σ) is the reciprocal of ρ .

For the analysis of the surface morphology, a White Light Interferometer (WLI) from Zygo New View 500 and SEM (JEOL 6400) were used.

Concerning optical characteristics, a CARY 5E UV-VIS-NIR spectrophotometer (Varian) was used to measure the transmission of the coatings, using air as reference.

Finally, the mechanical properties as adhesion and mechanical durability of the films were tested following standard procedures [17-19].

Results and Discussion

The electrical conductivity behaviour of coatings deposited on PC substrates using spin coating method and heated at 130 °C for 30 min as a function of the loading ratio of

the conducting fillers is shown for ITO nanoparticulate films (Fig. 1) and for carbon MWNTs films (Fig. 2). The maximum available loading ratio of carbon MWNTs was 0.6, as it was difficult to disperse more fillers in the colloid, because of the strong aggregation forming an unstable sol. In both layers, low electrical conductivity is observed at a small loading ratio which increases sharply at a certain loading ratio. However, it is observed that for carbon MWNTs films (Fig. 2) the increase of conductivity is sharper. At a higher loading ratio, the electrical conductivity increases smoothly and reaches a maximum value of (526 Sm^{-1}) for ITO nanoparticulate films and (65 Sm^{-1}) for carbon MWNTs films. This can be explained as a result of the higher content of the conductive filler which is available in the ITO based film.

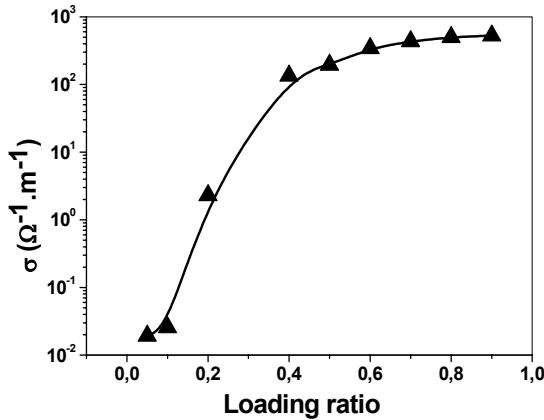


FIG. 1. The electrical conductivity of ITO based coatings onto a PC substrate as a function of the loading ratio of the ITO nanoparticles.

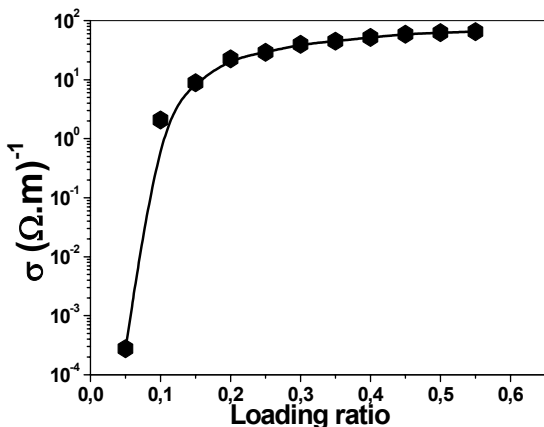


FIG. 2. The electrical conductivity of carbon MWNTs based coatings onto a PC substrate as a function of the loading ratio of the carbon MWNTs.

The electrical conductivity of the nanocomposite coatings was described by the classical percolation model, as

$$\sigma = \sigma_0 (V - V_c)^s$$

where σ is the direct electrical conductivity, σ_0 is the proportionality constant which represents the intrinsic electrical conductivity of the conductive filler, V is the conductive filler volume fraction, V_c is the percolation threshold at which the conductivity of the composite starts to increase sharply and s is the critical conductivity exponent.

To check if the composite conductivity follows the previous power law, a log-log plot of the electrical conductivity σ and $V - V_c$ is drawn as shown in Figs. 3 and 4. Fig. 3 shows that the data for ITO nanoparticulate films would fit very well the power law. The threshold percolation loading ratio (V_c) which gives the best linear fit is 0.19. The s value is determined as the slope of the least square fit line which is found to be 1.3. Compared with the system of the carbon MWNTs, a well fit of the experimental data is found, however with much lower percolation threshold of 0.083. The high aggregation of carbon nanotubes and their ability of forming ropes due to the van der Waal forces may explain the lower percolation threshold of the nanotubes system compared with that of the nanoparticulate system. It is observed that the nature of the conducting filler and the microstructure have a strong influence on the percolation threshold. The s value is found to be 1.2, which is close to the value found for the ITO nanoparticulate system. The exponent s measures the power of the conductivity increase above V_c .

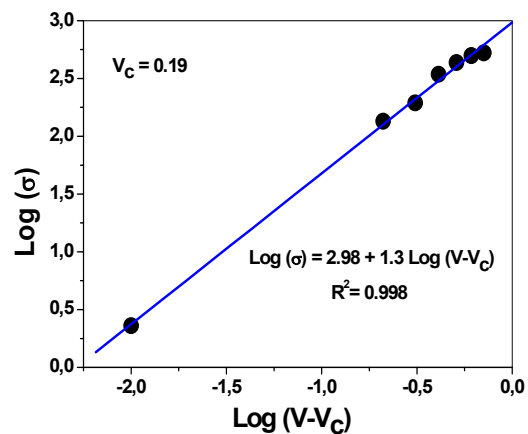


FIG. 3. Log-log graph of the conductivity and $V - V_c$ for ITO based layers.

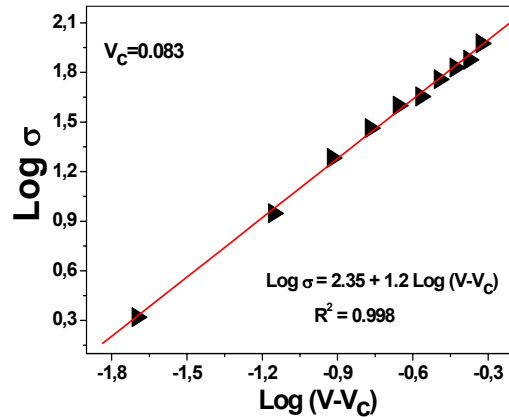


FIG. 4. Log-log graph for the conductivity and $V-V_c$ for MWNTs layers.

The explanation for such behaviour is attributed to the contact between the adjacent conductive fillers. Fig. 5 shows SEM micrograph of surface morphology of the ITO nanocomposite layers deposited on a PC substrate with different loading ratios. In the region of $V_c < 0.19$ (Fig. 5-a), a tiny segregated cluster is observed, as there are no contacts between the nanoparticles which are distributed separately within the host insulating matrix. By rising the nanoparticles concentration above the threshold percolation (Fig. 5-b), they begin to agglomerate and

touch each other forming a conductive network leading to a remarkable increase of the electrical conductivity of the coating. By further increment of the concentration of the ITO nanoparticles (Fig. 5-c), an observable morphology of the ITO network is shown which also results in an increase of the electrical conductivity of the film.

Fig. 6 shows WLI images for the surface of carbon MWNTs composite coatings with different loading ratios. Fig. 6-a shows a WLI surface image for a coating containing only 0.05 volume fraction of carbon MWNTs loading. It appears as an isolated cluster, which is different from the 0.15 volume fraction shown in Fig. 6-b, where an interconnected network of the nanotubes encapsulating within the insulating matrix appears on the surface. This interconnection explains the drastic increase of the electrical conductivity. Fig. 6-c shows the same image for 0.4 volume fraction, where a more homogeneous network of nanotubes was formed enhancing the electrical conductivity of the coatings.

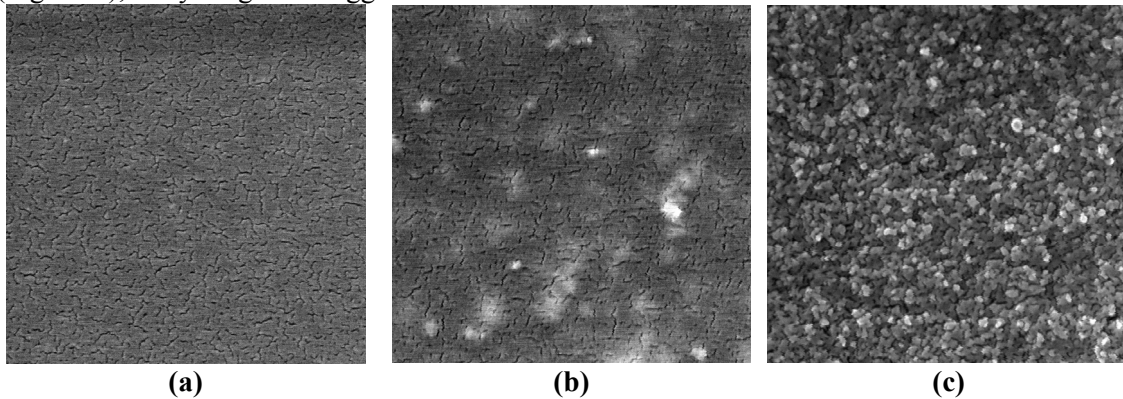


FIG. 5. The SEM surface morphology of GPTS_ITO layers with different ITO loading ratios: (a) 0.05, (b) 0.2 and (c) 0.9.

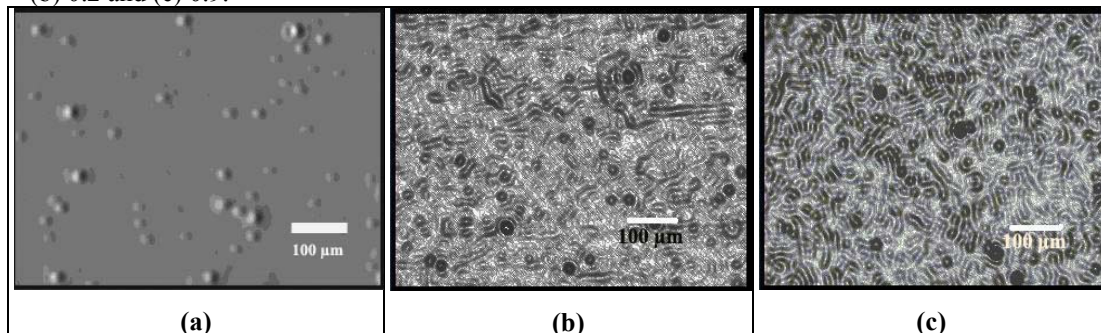


FIG. 6. WLI of the surface of GPTS_MWNTs layers for: (a) 0.05, (b) 0.15 and (c) 0.4 carbon MWNTs loading ratio.

Optical Properties

The transmission in the UV-VIS-NIR for the ITO based coatings and the carbon MWNTs on PC substrates was characterized as shown in Fig.7. Both coatings have a high transmission in the visible range; however that of ITO based layers shows higher transmission with smaller transmission

window. Furthermore, the ITO layer exhibits a sharp decrease in transmission around $\lambda = 1300$ nm showing almost no transmission in the NIR range. The main effect of this behaviour is due to the high absorption peak related to the presence of free carriers. It is also observed that both coatings exhibit high absorption in the UV region.

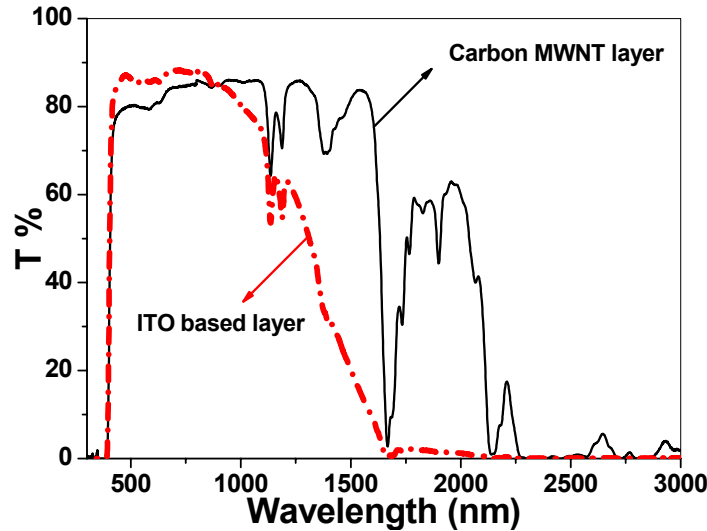


FIG. 7. The optical transmission in the UV-VIS-NIR range for ITO based layer and carbon MWNTs layer onto a PC substrate.

Mechanical Properties

The mechanical stability of the coatings is also an important factor to be taken into consideration. Both films gave excellent adhesion on polycarbonate substrates when tested with the tape test procedure (DIN 58196-K2). The resistance against abrasion was excellent according to the rubber test (DIN58196-G10). The hardness measured using the pencil test (ASTM D 3363-92a) ranged between 1H and 2H depending on the GPTS concentration with respect to the conducting fillers.

Conclusion

Nanocomposite thin films were deposited onto polymeric substrates using two coating colloids made of conductive ITO nanoparticles and carbon MWNTs. The electrical conductivity of both nanocomposite films exhibit a classical percolation law with a critical threshold of 0.083 for carbon MWNTs and 0.19 for ITO nanoparticles. The maximum obtained electrical conductivity for ITO films is $526 \Omega^{-1} \cdot m^{-1}$, which is larger than that obtained for the carbon MWNTs films ($65 \Omega^{-1} \cdot m^{-1}$). The ITO films show higher transmission than that of carbon MWNTs ones. Both types of films exhibit good mechanical durability against abrasion and scratch.

References.

- [1] Lewis, B.G. and Paine, D.C., *MRS Bulletin*, 25 (8) (2000) 22.
- [2] Chappel, S. and Zaban, A., *Solar Energy Materials and Solar Cells*, 71 (2002) 141.
- [3] Kim, V., Ku, Y., Lee, I., Seo, W., Cheong, K., Lee, T., Kim, I. and Lee, K., *Thin Solid Films*, 473 (2004) 315.
- [4] Shin, D., Kim, Y., Han, J., Moon, K. and Murakami, R., *Transactions of Nonferrous Metals Society of China*, 19 (2009) 997.
- [5] Al Dahoudi, N., PhD Thesis, (University of Saarland, 2003).
- [6] Jing, X., Zhao, W. and Lan, L., *Journal of Materials Science Letters*, 19 (2000) 377.
- [7] Flandin, L., Cavaillé, J.Y., Bidan, G. and Brechet, Y., *Polymer Composites*, 21(2) (2004) 165.
- [8] Ma, P., Liu, M., Zhang, H., Wang, S., Wang, R., Wang, K., Wong, Y., Tang, B., Hong, S., Paik, K. and Kim, J., *ACS Appl. Mater. Interfaces*, 1(5) (2009) 1090.
- [9] Lux, F., *Journal of Materials Science*, 28 (1993) 285.
- [10] Clerc, J.P., Giraud, G., Laugier, J.M. and Luck, J.M., *Adv. Phys.* 39 (1990) 191.
- [11] Hartnagel, H., Dawar, A., Jain, A. and Jagadish, C., *Semi-conducting Transparent Thin Films*, (Institute of Physics Publishing, 1995).
- [12] Chung, J., Choi, B. and Lee, H., *Appl. Phys. Lett.* 74 (1999) 3645.
- [13] Arias, A., Gransröm, M., Thomas, D., Petritsche, K. and Friend, R., *Phys. Rev. B*, 60(3) (1999) 1854.
- [14] Kaempgen, M., Duesberg, G.S. and Roth, S., *Applied Surface Science*, 252 (2005) 425.
- [15] Bradford, P. and Bogdanovich, A., *Journal of Composite Materials*, 42 (15) (2008) 1533.
- [16] Wu, Z., Chen, Z., Du, X., Logan, J.M., Sippel, J., Nikolou, M., Kamaras, K., Reynolds, J.R., Tanner, D.B., Hebard, A.F. and Rinzler, A.G., *Science* 305 (2004) 1273.
- [17] Tape Test Procedure DIN 58196-K2.
- [18] Abrasion Resistance Test, DIN58196-G10.
- [19] Pencil Test ASTM D 3363-92a.

AFM Study of Multilayer Sol-gel $\text{Ba}_x\text{Sr}_{1-x}\text{TiO}_3$ Thin Films

Ala'eddin A. Saif, N. Ramli and P. Poopalan

Microfabrication Cleanroom, School of Microelectronic Engineering, University Malaysia Perlis (UniMAP), Kuala Perlis, 02000, Perlis, Malaysia.

Received on: 15/3/2010; Accepted on: 5/9/2010

Abstract: Multilayer Barium Strontium Titanate (BST) sol-gel films with molar formula $\text{Ba}_x\text{Sr}_{1-x}\text{TiO}_3$ ($x = 0.5, 0.7$ and 0.8) are deposited on SiO_2/Si substrates. The surface morphology and grain size are characterized via Atomic Force Microscope (AFM), showing the films to be uniform and crack-free. The average roughness, maximum peak to valley height, root mean square (RMS) roughness, ten-point mean height roughness, surface skewness and surface kurtosis parameters are used to analyze the surface morphology of the BST thin films. Generally, the results show that the surface roughness increases with decreasing Sr content with RMS roughness increasing from 4.77 nm to 6.52 nm for films of 160.8 nm thickness as Sr content decreases. Surface roughness also increases with the film thickness, for $x = 0.5$, RMS roughness increases from 4.77 nm to 13.33 nm as the film thickness increases from 160.8 nm to 446.8 nm. A similar trend for surface roughness is obtained, for all x values, as is for grain size.

Keywords: BST; Thin film; Sol-gel; AFM; Surface roughness.

PACS: 68.37.Ps; 68.55.J-; 81.20.Fw; 77.55.fe.

Introduction

Ferroelectric Barium Strontium Titanate (BST) thin films have been widely investigated as a potential material for use in microelectronic devices such as non-volatile random access memory (RAM) and ferroelectric field effect transistor (FeFET) due to its high dielectric constant, as well as relatively low dielectric loss tangent. Furthermore, its desirable pyroelectric and piezoelectric properties can be utilized for a variety of sensing applications [1, 2]. Therefore, a large number of studies have been conducted to improve the quality of BST thin films. An important factor in all the applications of BST is its surface structure. Hence, it is imperative to have a good understanding of the surface morphology of BST thin films for fabrication of advanced microelectronics devices [3].

Surface morphology plays an important role in various areas of science and

technology [4]. It can be used to understand many fundamental problems such as friction, contact deformation, heat and electric current conduction [5]. There are many parameters used to evaluate the surface roughness. These parameters are categorized into three groups: amplitude, spatial and hybrid parameters; however, the most important group is the amplitude parameters [6].

Relatively few studies have focused on the surface roughness of BST thin films. C. Fu *et al.* showed that the grain size and surface roughness increase as the annealing temperature increases [7]. Wencheng Hu *et al.* reported that BST film surface roughness increases with the concentration of precursor solutions [8]. In this work, BST thin films of different Ba:Sr content and different film thicknesses are prepared by the sol-gel technique, and the surface roughness and the grain sizes for these films are determined

using an atomic force microscope (AFM). A comprehensive analysis of the BST surface properties using parameters such as the average roughness, maximum peak to valley height, root mean square roughness, ten-point mean height roughness, surface skewness and surface kurtosis is made. These are parameters that allow insight into the surface properties and quality.

BST Films Preparation

Different values of Ba:Sr content, x , of the $Ba_xSr_{1-x}TiO_3$ solutions were prepared by sol-gel method. Barium acetate, strontium acetate and titanium (IV) isopropoxide were used as starting materials, with glacial acetic acid and 2-Methoxyethanol as solvents. Specific amounts of barium acetate and strontium acetate were dissolved in 10 ml heated acetic acid to obtain the Ba-Sr solution. A stoichiometric amount of titanium (IV) isopropoxide was added to 4ml 2-Methoxyethanol to get a separate solution. Both solutions were then mixed and refluxed separately with the Ba-Sr solution being drip-added to the titanium solution. The final mixture was magnetically stirred at 400 rpm for two hours and refluxed to get a thick solution, which was filtered using a nylon microfiber filter. Three different solutions with Ba:Sr proportions of 50:50, 70:30 and

80:20 were prepared, and labeled BST50, BST70 and BST80, respectively.

BST thin films were spun layer by layer on SiO_2/Si substrates with a specific heating procedure. For each layer, the as-deposited BST thin film was baked at 200 °C for 20 min to vaporize the organic solvents. Then, it was heated at 500 °C for 30 min in an O_2 atmosphere before the next layer was spun-on. This process was repeated until four layers were deposited. Finally, the BST films were annealed at 800 °C for 1 h in an O_2 atmosphere. Films with one, two, three and four layers for each Ba:Sr ratio were prepared with the same procedure.

Measuring Method

The AFM (SPA400, SII Nanotechnology, Inc.) was operated in contact mode, with a 2.9 μm high tip, less than 20 μm in radius and with a cone angle less than 70°. There are two cantilevers, denoted as A and B, with individual parameters as summarized in Table 1. In contact mode scanning, the low spring constant of the cantilever, which is less than the effective spring constant holding the atoms of the sample together, allows the tip to trace across the sample gently providing high resolution image of the surface compared to tapping mode.

TABLE 1. The dimensions and the mechanical properties of the cantilevers used.

	Cantilever A	Cantilever B
Length (L/ μm)	200	100
Width (W/ μm)	166 (base) to 6 (head)	106 (base) to 6 (head)
Thickness (t/ μm)	0.4	0.4
Resonance frequency (kHz)	11	34
Spring constant (N/m)	0.02	0.08

In order to completely characterize the surface, at least 3 images, with an area of 10 $\mu m \times 10 \mu m$ using cantilever A and scanned at 2 Hz, were recorded for different positions to avoid the edge effect. However, for grain size investigation, the measurement area was reduced to 500 nm \times 500 nm with cantilever B and a 2 Hz scan speed. Specific roughness parameters were extracted using Gwyddion software [9].

In order to measure the film thickness, the films were partially dipped in diluted hydrofluoric acid (HF); the resulting step-profile thickness was measured with a stylus profilometer. The thicknesses of one, two, three and four layers of BST50 films were: 149.5 nm, 226.6 nm, 356.8 nm and 435.2 nm, respectively, and for BST70 films: 160.8 nm, 235.6 nm, 368.5 nm and 446.8 nm, respectively, and for BST80 films: 165.4 nm, 247.1 nm, 374.6 nm and 449.3 nm, respectively. However, the BST70 values were taken as the reference benchmark for all of the BST ratios in this article.

AFM Amplitude Analysis

The amplitude parameters of a sample are described by parameters which give information about statistical average values, shape of the histogram heights and other extreme properties.

The average roughness (R_a) is the mean height as calculated over the entire measured length/area. Maximum peak to valley height roughness (R_t) is the vertical distance between the highest and lowest points in the evaluated length/area and describes the overall roughness of the surface. Root mean square (RMS) roughness (R_q) is the square root of the distribution of surface height and is considered to be more sensitive than the average roughness for large deviations from the mean line/plane and is also used in computing the skew and kurtosis parameters. Ten-points mean height roughness (R_z) is the difference in height between the average of five highest peaks and five lowest valleys in the evaluation profile/surface and is more sensitive to occasional high peaks or deep valleys than R_a . Roughness skewness (R_{sk}) is used to measure the symmetry of the variations of a profile/surface about the mean line/plane and is more sensitive to occasional deep valleys or high peaks. Usually, R_{sk} is used to distinguish two profiles of the same R_a or R_q values but of different shapes. Roughness kurtosis (R_{ku}) is used to measure the distribution of the spikes above and below the mean line/plane.

Results and Discussion

The microstructure, such as the grain size and the surface roughness, is one of the key parameters determining the electrical properties of high dielectric constant thin films [10]. The electrical properties of BST thin films are closely linked to the microstructure of the films such as grain size, cracks, pinholes and roughness [11]. Hence, if the grain size of the BST thin films is large, the dielectric constant may be similar to that of the bulk BST [12].

Conventional Metal-Ferroelectric Metal (MFS) structures have many problems such as difficulty in depositing ferroelectric thin films directly on silicon, high trap densities and diffusion of elements into silicon. However, incorporating MFS structures in standard CMOS processes will benefit from the usage of Si-substrates and plethora of established techniques for reduced fabrication cost. A possible solution for these problems is to use a buffer layer between the ferroelectric thin film and silicon [13]. SiO₂ layer has been used as the buffer in this research. Fig. 1 shows the cross-sectional view of BST80 film, 446.8 nm in thickness.

Fig. 2 shows the three-dimensional AFM micrographs of the surface of BST50, BST70 and BST80 single layer films with 160.8 nm thickness. The micrographs reveal that the films do not show continuous long trenches or blotches, which are indicative of a crack free and pinhole-free surface.

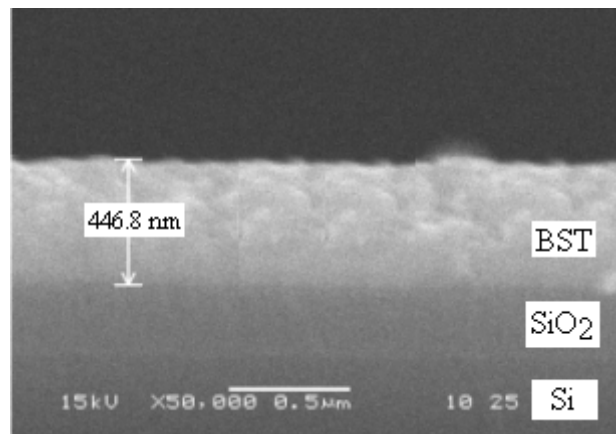


FIG. 1. SEM micrograph of the cross-section of BST80 film deposited on SiO₂/Si substrate.

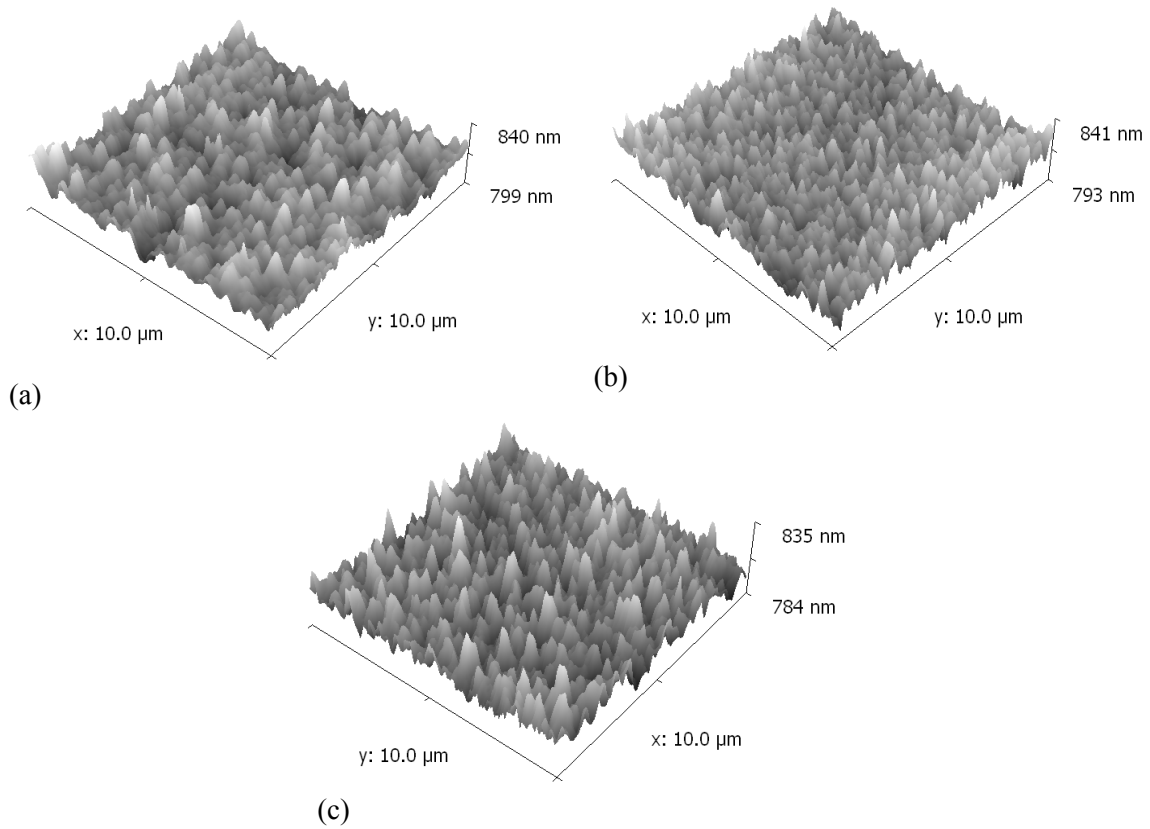


FIG. 2. Three dimensional AMF micrograph for a) BST50, b) BST70 and BST80 thin films with 160.8 nm thickness.

The variations of the root mean square roughness (R_q) of the BST50, BST70 and BST80 films as a function of the film thickness are shown in Fig. 3. The RMS roughness increases with film thickness almost linearly, as well as with increasing Ba

content. The increase in R_q for high Ba content films is due to the size difference between Ba^{2+} ions ($r = 0.135$ nm) and Sr^{2+} ions ($r = 0.113$ nm). The rest of the roughness parameters of the tested samples is summarized in Table 2.

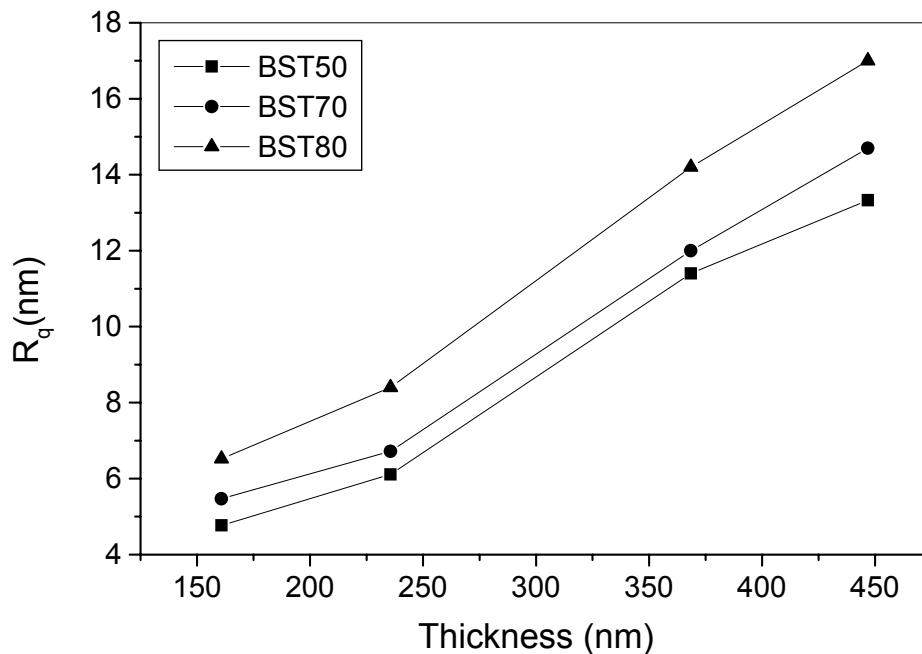


FIG. 3. Variations of the root mean square roughness for different thicknesses of BST films (BST50, BST70 and BST80).

Table 2 illustrates that the variations of the average roughness values (R_a) and ten-point mean height (R_z) values have the same trend as the variations of RMS roughness (R_q) values for all molar ratios and thicknesses. Maximum peak to valley height (R_t) is also considered a very important parameter because it gives a good description of the overall roughness of the surface. The results from the Table show that R_t is high for BST70 and BST80 compared to BST50, which means that the surface roughness increases with Ba content, indicating that as Ba content increases bigger individual unit cells lead to larger clumps of grains. R_t also shows notable increments as the film thickness of BST50 increases. BST70 and BST80 samples lack this trend for films with three and four layers. The Table also shows that for high values of R_t , R_z is also high due to the strong dependence of R_z on the peak heights / valley depths. R_z is mathematically given by the following formula [5]:

$$R_z = \frac{1}{n} \left(\sum_{i=1}^n P_i - \sum_{i=1}^n V_i \right) \quad (1)$$

where n is the number of sampling points along the assessment length, which is 5 in this study, P_i is the height of the i -th peak and V_i is the depth of the i -th valley with respect to the line profile.

In addition, R_q values for all the samples are higher than R_a values, which can be mathematically explained according to the following equations [5].

$$R_a = \frac{1}{L} \int_0^L |y(x)| \cdot dx \quad (2)$$

$$R_q = \sqrt{\frac{1}{L} \int_0^L (y(x))^2 \cdot dx} \quad (3)$$

where L is the length of the profile on the x -axis used for measurement and $y(x)$ is the variation of the height from the profile line for each data point.

TABLE 2. The roughness parameters of BST50, BST70 and BST80 at different thicknesses.

Sample	Thickness (nm)	R_a (nm)	R_t (nm)	R_q (nm)	R_z (nm)	R_{sk}	R_{ku}
BST50	160.8	3.65	27.6	4.77	16.43	0.35	3.93
	235.6	4.65	38.9	6.11	20.94	-0.25	3.19
	368.5	9	59.4	11.4	34.69	0.19	3.60
	446.8	10.59	65.4	13.33	43.8	0.43	3.08
BST70	160.8	4.33	29.6	5.47	17.94	0.14	3.21
	235.6	5.25	36.81	6.72	21.41	0.25	3.57
	368.5	9.16	124	12	48.4	1.37	11.17
	446.8	11.2	95.4	14.7	56.2	0.21	5.85
BST80	160.8	5.14	32.5	6.52	22.1	0.46	3.36
	235.6	6.6	45.1	8.4	24.2	0.325	3.38
	368.5	9.7	116.7	14.2	57.2	-0.05	8.77
	446.8	13.4	92.41	17	58.47	0.29	3.34

In Table 2, negative values of the skewness indicate that the valleys are dominant over the scanned area and positive values show that the peaks are dominant on the surface. Continued negative values would indicate cracks, representative of valleys. The distribution of positive and negative values indicates the existence of protruding grains. For kurtosis, an R_{ku} below three shows that the distribution over the scanned area has relatively few high peaks and low valleys, which means a bumpy surface. When R_{ku} is

more than three, the distribution will have relatively higher numbers of high peaks and low valleys, characteristic of a spiky surface [5]. The results of skewness and kurtosis show that the BST surface generally is spiky with peaks being dominant. Films with high R_{ku} values have high R_t and R_z values as well. This is due to the strong relation between these parameters, where R_{ku} is, mathematically, directly related to the peak heights and valley depths according to the following formula [5].

$$R_{ku} = \frac{1}{NR_q^4} \left(\sum_{i=1}^N Y_i^4 \right) \quad (4)$$

where R_q is the RMS roughness parameter and Y_i is the height of the profile at point number i .

Fig. 4 shows a two-dimensional AFM micrograph with $500 \times 500 \text{ nm}^2$ scanned area for different thicknesses of BST50, BST70 and BST80 films. The grain distribution is uniform for all three types. The values of the

grain sizes for BST50, BST70 and BST80 films are plotted against film thickness, as illustrated in Fig. 5. It is clearly seen that the grain size increases with increasing Ba content and film thickness. The increase of the grain size in high Ba content films is due to the fact that Ba has a larger ionic radius which causes a larger crystalline unit cell, which in turn causes larger clumps of unit cells or grains.

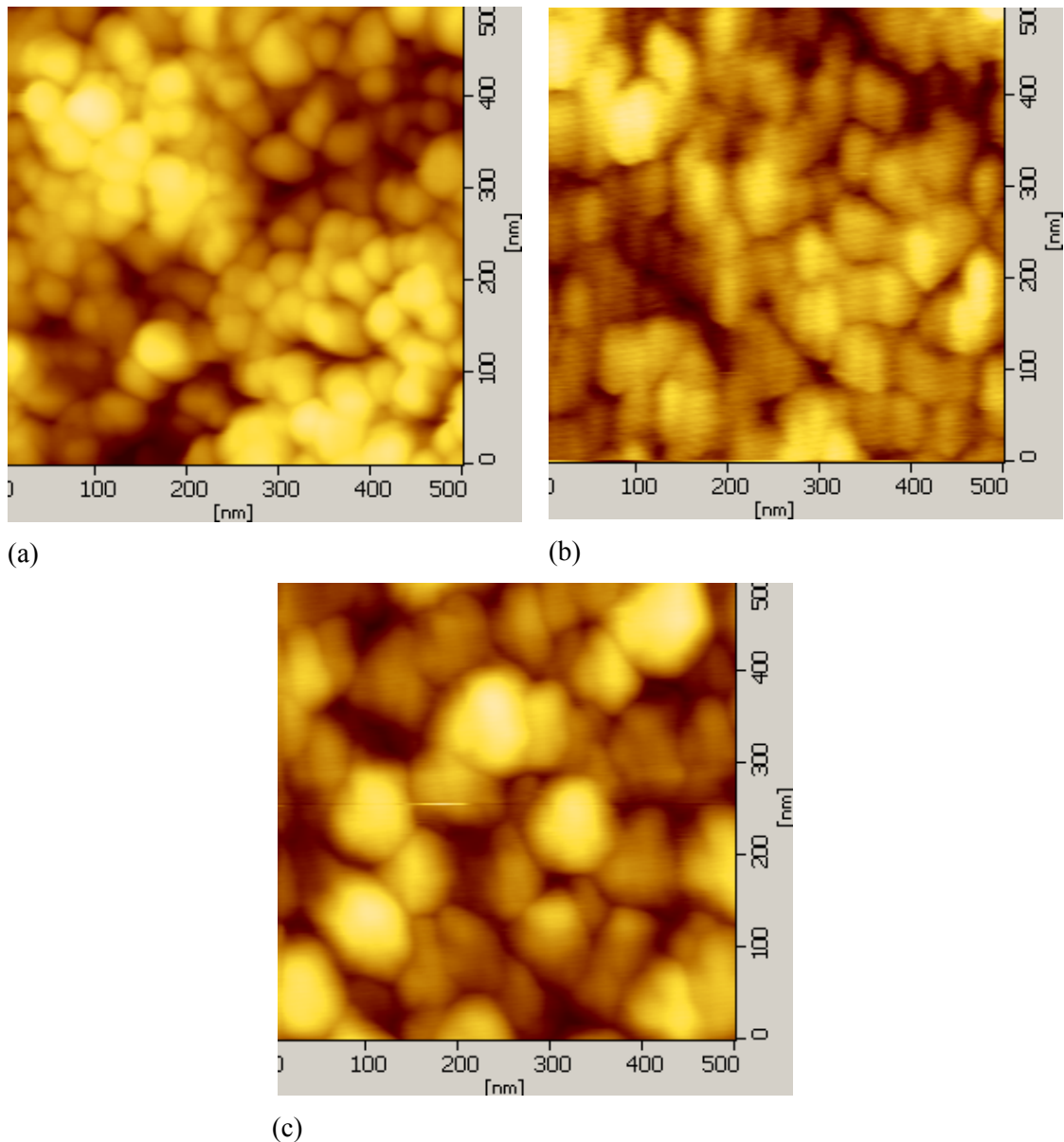


FIG. 4. Two-dimensional AFM micrograph of a) BST50, b) BST70 and c) BST80 films showing the distribution of the grains.

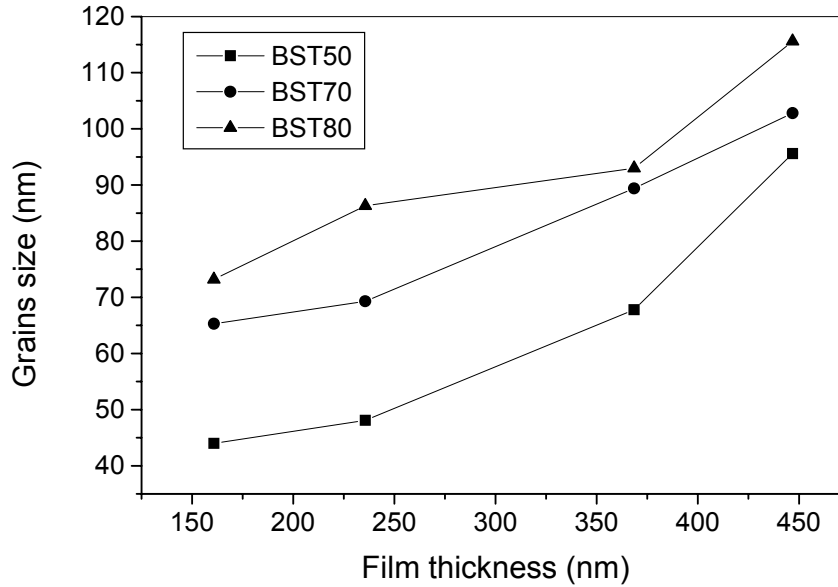


FIG. 5. The variation of grain size with film thickness for different Ba-Sr molar contents.

Adding Sr^{2+} ions to BST changes the unit cell volume, where Strontium ions are introduced at the A site of the perovskite matrix and enter substitutionally into the Ba^{2+} ion sites [14]. The small size of Sr^{2+} ions causes the unit cell to become smaller. This substitution of ions will also affect the dielectric and electrical properties of BST. As the number of Sr^{2+} ions increase in the lattice, a smaller unit cell will be obtained which leads to smaller grain growth during annealing. The bright grains appearing in the AFM images in Fig. 4 represent grains closer to the surface.

The increase in surface roughness and grain size with the increase in film thickness is due to grain growth during the deposition and annealing process of the layers. During deposition, the film is heated at $500\text{ }^\circ\text{C}$ for 30 min after each layer, this temperature is enough to grow the BST grains, so the next layer deposition is carried out over films with established grain boundaries and the solution is randomly spread over all these grains, so bigger grains will be obtained after the heating and annealing of the new layer.

The results of the surface roughness and the grain size show that their values can be controlled by adjusting the Ba-Sr ratio and the number of layers deposited. Furthermore, changing the number of layers deposited has a more significant effect on grain size than that due to Ba-Sr ratio (for the same thickness).

Conclusion

Multilayer Barium Strontium Titanate (BST) films with the molar formula $\text{Ba}_x\text{Sr}_{1-x}\text{TiO}_3$ ($x = 0.5, 0.7$ and 0.8) have been fabricated on SiO_2/Si substrates by sol-gel technique. The surface morphology and the grain size are characterized via Atomic Force Microscope (AFM). The results show that the sol-gel technique has a high efficiency in fabricating high quality BST thin films on SiO_2/Si substrates, as shown by the very dense, crack-free films formed with low surface roughness and possessing relatively large grain sizes. Generally, the surface roughness increases as Sr content decreases ($1-x$ value), where the root mean square roughness increases from 4.95 nm to 6.9 nm for films of 160.8 nm thickness as Sr content decreases. The surface roughness also increases as the number of layers (film thickness) increases, for $x = 0.5$, RMS roughness increases from 4.95 nm to 13.5 nm as the film thickness increases from 160.8 nm to 446.8 nm . A similar trend for surface roughness is obtained, for all x values, as is for grain size. The values of surface roughness and grain size can be controlled by adjusting the Ba-Sr ratio and the number of deposited layers. Surface roughness and grain size for all samples show a direct relation between each other where the surface roughness shows an increasing trend as the grain size increases. The BST surface is dominated by peaks with lots of high peaks and low valleys.

References

- [1] Hongwei, C., Chuanren, Y., Chunlin, F., Li, Z. and Zhiqiang, G., *Appl. Surf. Sci.* 252 (2006) 4171.
- [2] Li, G., Yu, P. and Xiao, D., *J. Electroceram.* 21 (2008) 340.
- [3] Cui, D., Lu, H., Wang, H. and Tao, H., *Chin. Phys. Lett.* 14 (1997) 134.
- [4] Bałamucki, J., Czarnecki, P., Gotszalk, T. and Kowalski, Z.W., *Phys. Chem. Sol. State.* 8 (2007) 583.
- [5] Gadelmawlaa, E.S., Kourab, M.M., Maksoudc, T.M.A., Elewaa, I.M. and Solimand, H.H., *J. Mater. Process. Tech.* 123 (2002) 133.
- [6] Wysocka, K., Ulatowska, A., Bauer, J., Holowacz, I., Savu, B. and Stanciu, G., *Optica Applicata.* XXXVIII (2008) 130.
- [7] Chunlin, F., Chuanren, Y., Hongwei, C., Liye, H. and Yingxin, W., *Mater. Lett.* 59 (2005) 330.
- [8] Wencheng, H., Chuanren, Y., Wanli, Z. and Lin, Z., *Integ. Ferroelect.* 72 (2005) 1.
- [9] Personal communications with Mr. David Necas to modify Gwyddion software to fit with SII nanotechnology Ins AFM images format.
- [10] Ru-Bing, Z., Chun-Sheng, Y., Gui-Pu, D. and Jie, F., *Mater. Res. Bull.* 40 (2005) 1490.
- [11] Mazon, T., Zaghete, M.A., Varela, J.A. and Longo, E., *J. Eur. Ceram. Soc.* 27 (2007) 3799.
- [12] Qin, W.F., Xiong, J., Zhu, J., Tang, J.L., Jie, W.J., Wei, X.H., Zhang, Y. and Li, Y.R., *J. Mater. Sci: Mater. Electron.* 18 (2007) 973.
- [13] Woo-Sik, K., Su-Min, H., Jun-Kyu, Y. and Hyung-Ho, P., *Thin Solid Films*, 398–399 (2001) 663.
- [14] Patil, D.R., Lokare, S.A., Devan, R.S., Chougule, S.S., Kanamadi, C.M., Kolekar, Y.D. and Chougule, B.K., *Mater. Chem. Phys.* 104 (2007) 254.

Jordan Journal of Physics

ARTICLE

Ionosphere Scintillation and Earthquakes

R. A. Kandalyan and M. Kh. Alquran

*Institute of Astronomy and Space Sciences (IASS), Al al-Bayt University, P.O. Box 130040,
Al-Mafraq, 25113, Jordan.*

Received on: 15/02/2010; Accepted on: 11/10/2010

Abstract: Recent theoretical and experimental studies demonstrated the ability of space technologies to identify and monitor the specific variations at near-earth space plasma and atmosphere associated with approaching severe earthquakes, named as earthquake precursors, which appear several days before the seismic shock over the seismically active areas [1].

This paper aims at determining the relationship between ionosphere scintillation of radio waves and earthquakes.

Data for GPS (Global Positioning System) S_4 index have been examined through spatial and temporal correlation. The results showed that the pre-seismic activity can be considered as a source of ionosphere scintillation.

Keywords: Space plasma; Ionosphere; Scintillation; Earthquakes.

PACS: 94.05-a, 94.20-y, 91.30 px.

Introduction

Earthquakes are the most fatal natural disasters. Natural tectonic earthquakes are uncontrollable by humans. Therefore the best way to avoid these natural disasters is to predict their occurrence and take precautions. There are many indications that can be observed before an earthquake strikes. These are called precursors. According to Pulnits and his collaborators [2, 3], the scale height changes in the vertical distribution of ions and electrons within the F-layer of ionosphere are due to seismogenic effects.

The critical frequency f_oF_2 layer data are analyzed with upper and lower bound of inter-quartile range (IQR) and the observed anomalous changes are related to geomagnetic disturbances [4]. The results of the study show some unusual perturbations observed in critical frequency f_oF_2 region, 1–25 days before and 2–3 days after the main shock.

An additional study shows that critical frequency is reduced both in the pre- and post-midnight hours 0 – 4 days and 1–15 days

before the occurrence of earthquakes, respectively. The reduction varies between 24% and 35% in the pre-midnight sector and between 18% and 30% in the post-midnight sector [5].

The mechanism of ULF (Ultra Low Frequency) geomagnetic oscillations is based on the formation of periodic structure of ionosphere conductivity due to acoustic gravity wave instability stimulated by electric field enhancement in the ionosphere [6].

The wave measurements detected by the SORS (Solar Radio Spectrometer) instrument in the 0.1–15 MHz frequency range, as well as the gamma ray fluxes in the energy ranges of 0.12–0.32 and 3.0–8.3 MeV, detected by the SONG (Solar Neutron and Gamma Rays Device) instrument, located on the low orbiting satellite CORONAS-I (Complex Orbital Near-Earth Observations of the Solar Activity) were used to present the ionosphere plasma response to strong seismic activity on 31.03.1994 during quiet geomagnetic conditions and on 6.04.1994 during a

geomagnetic storm period [7]. In order to better understand the physical conditions and the physical processes in the ionosphere plasma, the characters of typical ionosphere parameters are registered by a network of ground-based ionosondes [8].

In this paper, the ionosphere scintillation index S_4 is thoroughly examined to determine the relationship between scintillation and occurrence of seismic activities. The GPS observations were carried out at a frequency of 1.575 GHz. We tested S_4 index on 3 separate earthquakes in Indonesia, as well as an earthquake in the United States. In the following section, data and results are presented. Then, an analysis of the observed correlation is presented. The conclusion is presented in the last section.

Data and Results

The S_4 index is a statistical parameter; namely the standard deviation of the received power of the signal coming from GPS satellite passing through the ionosphere normalized by its mean value.

$$S_4 = \frac{(\langle P^2 \rangle - \langle P \rangle^2)^{1/2}}{\langle P \rangle}$$

where P is the received power of the signal coming from the satellite. It is the most commonly used parameter for indicating the intensity variation.

The severity of the earthquake can be described according to Dobrovolsky's empirical formula [9]

$$\rho = 10^{0.43M} \text{ km}$$

where ρ is the radius of the preparation zone of the earthquake and M is the earthquake's magnitude. Previously, no earthquake severity under a magnitude of 6.0 was tested. This is due to the fact that an earthquake of a magnitude of 6.0 or lower cannot generate enough impact to affect the ionosphere [2].

For data collection, the following steps are completed.

1. We determine the coordinates (longitude/latitude) of the GPS receiver's location.
2. We collect information of earthquakes within a circular region with a radius of about 7000 km, its median point being the GPS receiver, using Earthquake Hazard Program [10]. The lower limit of earthquake's magnitude $M = 6$ is adopted.
3. Upon selection of the earthquake that affects the GPS receiver, we compare the distance between the earthquake's center and the location of the GPS receiver. On the other hand, we estimate the radius of the region affected by the earthquake (according to Dobrovolsky's formula [9]). When both distances are comparable, we include that earthquake in our analysis. Following this procedure, just few earthquakes are selected, which are shown with their characteristics in Table 1.
4. As for S_4 index, data are available from GPS Scintillation Data in Indonesia web site which belongs to Solar-Terrestrial Environment Laboratory/ Nagoya University [11]. Additional data are available from the web site that belongs to Bear Lake Observatory/ Utah State University [12].

TABLE 1. Characteristics of the selected earthquakes.

Number	Date	Time	Latitude in degrees	Longitude in degrees	Magnitude	Distance from receiver (km)
1	22/2/2004	6:46	-1.56	100.49	6.0	180
2	11/5/2004	8:28	0.41	97.82	6.1	245
3	25/7/2004	14:35	-2.43	103.98	7.3	517
4	15/6/2005	2:51	41.29	-125.95	7.2	1228

The severe scintillations with $S_4 > 0.5$ are selected.

If we attempt to analyze data from earthquakes in a period of time that is too long, we will not be able to see the deeper

details. On the other hand, if we take a look at data from earthquakes in a period of time that is too short, we will not be able to collect enough information. We have found that a two-to three-month period of time proves to be an excellent interval.

For the earthquake in Indonesia that occurred on 22/2/2004, S_4 data were collected for the period between 1/1/2004 and 1/3/2004 (Table 2), and those of Indonesia earthquake of 11/5/2004 were collected for the period between 1/3/2004 to 31/5/2004 (Table 3). With respect to Indonesia earthquake of

25/7/2004, S_4 data were selected for the time interval between 1/6/2004 and 31/8/2004 (Table 4). Those of Utah State earthquake of 15/6/2005 were collected between 1/5/2005 and 31/7/2005 and are presented in Table 5. Columns of Tables 1 to 5 are self-explanatory.

TABLE 2. Number of severe scintillations for the period from 1/1/2004 to 1/3/2004 which includes Indonesia earthquake of 22/2/2004.

Date	No. of severe scintillations	Date	No. of severe scintillations
1	2	3	4
1/1/2004	8	1/2/2004	7
2/1/2004	4	2/2/2004	9
3/1/2004	2	3/2/2004	7
4/1/2004	2	4/2/2004	6
5/1/2004	5	5/2/2004	12
6/1/2004	1	6/2/2004	10
7/1/2004	3	7/2/2004	13
8/1/2004	2	8/2/2004	14
9/1/2004	5	9/2/2004	14
10/1/2004	4	10/2/2004	18
11/1/2004	6	11/2/2004	21
12/1/2004	4	12/2/2004	19
13/1/2004	5	13/2/2004	18
14/1/2004	4	14/2/2004	16
15/1/2004	4	15/2/2004	15
16/1/2004	4	16/2/2004	14
17/1/2004	3	17/2/2004	14
18/1/2004	7	18/2/2004	16
19/1/2004	5	19/2/2004	n.a.
20/1/2004	5	20/2/2004	13
21/1/2004	8	21/2/2004	18
22/1/2004	8	22/2/2004	19
23/1/2004	6	23/2/2004	13
24/1/2004	5	24/2/2004	13
25/1/2004	7	25/2/2004	13
26/1/2004	5	26/2/2004	15
27/1/2004	n.a.	27/2/2004	9
28/1/2004	n.a.	28/2/2004	7
30/1/2004	6	1/3/2004	7
31/1/2004	5		

The relationships between scintillation S_4 indices (left axis), earthquake magnitude (right axis) and time for Indonesia earthquakes on 22/02/2004, 11/05/2004 and 25/07/2004 are presented in Figure 1, based on Tables 2 to 4. Figure 2 shows the same relationships for Utah earthquake based on Table 5. The tight correlation between occurrence of earthquakes and severity of ionosphere scintillation is evident.

From (Figs. 1 and 2), we can see that the daily number of occurrences for severe scintillations begins to increase approximately two weeks before the main shock, as well as a few days after it. This is due to the fact that there are pre-seismic activities preceding the earthquake, as well as relay waves (acoustic waves that travel through the atmosphere and reach the ionosphere) following the earthquake.

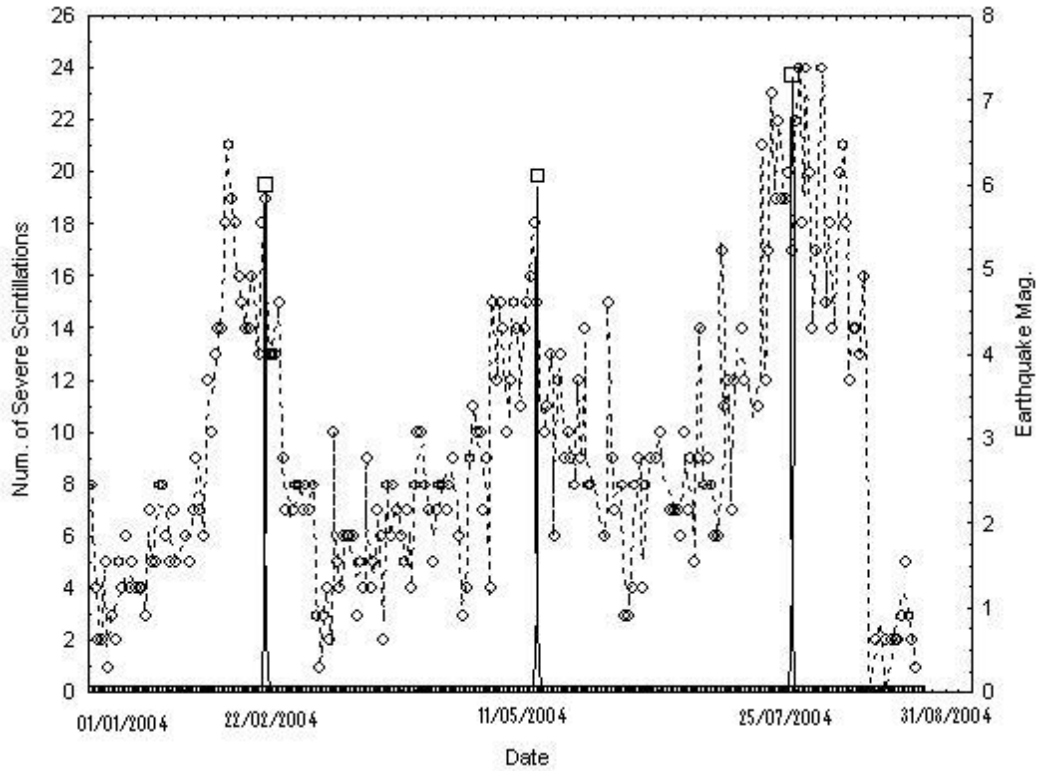


FIG. 1. The relationship between the number of severe scintillations (left axis) represented by circles and the magnitude of an earthquake (right axis) represented by squares. The results for Indonesia earthquakes of 22/2/2004, 11/5/2004 and 25/7/2004 are presented.

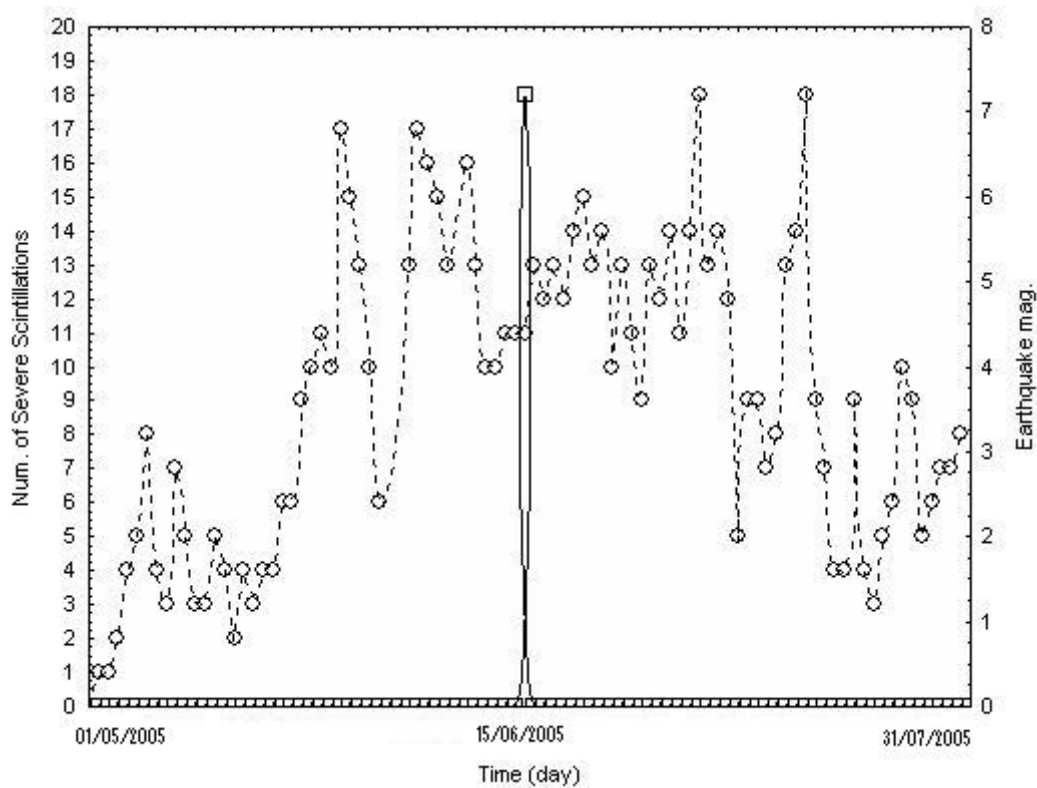


FIG. 2. The relationship between the number of severe scintillations (left axis) represented by circles and the magnitude of an earthquake (right axis) represented by squares. Shown are the results for Utah State earthquake of 15/6/2005.

TABLE 3. Number of severe scintillations for the period from 1/3/2004 to 31/5/2004 which includes Indonesia earthquake of 11/5/2004.

Date	No. of severe scintillations	Date	No. of severe scintillations
1	2	3	4
1/3/2004	8	16/4/2004	9
2/3/2004	8	17/4/2004	n.a.
3/3/2004	7	18/4/2004	6
4/3/2004	8	19/4/2004	3
5/3/2004	7	20/4/2004	4
6/3/2004	8	21/4/2004	9
7/3/2004	3	22/4/2004	11
8/3/2004	1	23/4/2004	10
9/3/2004	3	24/4/2004	10
10/3/2004	4	25/4/2004	7
11/3/2004	2	26/4/2004	9
12/3/2004	10	27/4/2004	4
13/3/2004	5	28/4/2004	15
14/3/2004	4	29/4/2004	12
15/3/2004	6	30/4/2004	15
16/3/2004	6	1/5/2004	14
17/3/2004	6	2/5/2004	10
18/3/2004	6	3/5/2004	12
19/3/2004	3	4/5/2004	15
20/3/2004	5	5/5/2004	14
21/3/2004	4	6/5/2004	11
22/3/2004	9	7/5/2004	14
23/3/2004	4	8/5/2004	15
24/3/2004	5	9/5/2004	16
25/3/2004	7	10/5/2004	18
26/3/2004	6	11/5/2004	15
27/3/2004	2	12/5/2004	n.a.
28/3/2004	8	13/5/2004	10
29/3/2004	6	14/5/2004	11
30/3/2004	8	15/5/2004	13
31/3/2004	7	16/5/2004	6
1/4/2004	6	17/5/2004	12
2/4/2004	5	18/5/2004	13
3/4/2004	7	19/5/2004	9
4/4/2004	4	20/5/2004	10
5/4/2004	8	21/5/2004	9
6/4/2004	10	22/5/2004	8
7/4/2004	10	23/5/2004	12
8/4/2004	8	24/5/2004	9
9/4/2004	7	25/5/2004	14
10/4/2004	5	26/5/2004	8
11/4/2004	7	27/5/2004	8
12/4/2004	8	28/5/2004	n.a.
13/4/2004	8	29/5/2004	n.a.
14/4/2004	7	30/5/2004	n.a.
15/4/2004	8	31/5/2004	6

TABLE 4. Number of severe scintillations for the period from 1/6/2004 to 31/8/2004 which includes Indonesia earthquake of 25/7/2004.

Date	No. of Severe scintillations	Date	No. of Severe scintillations
1	2	3	4
1/6/2004	15	17/7/2004	12
2/6/2004	9	18/7/2004	17
3/6/2004	7	19/7/2004	23
4/6/2004	n.a.	20/7/2004	19
5/6/2004	8	21/7/2004	22
6/6/2004	3	22/7/2004	19
7/6/2004	3	23/7/2004	19
8/6/2004	4	24/7/2004	20
9/6/2004	8	25/7/2004	17
10/6/2004	9	26/7/2004	22
11/6/2004	4	27/7/2004	24
12/6/2004	8	28/7/2004	18
13/6/2004	9	29/7/2004	24
14/6/2004	n.a.	30/7/2004	20
15/6/2004	9	31/7/2004	14
16/6/2004	10	1/8/2004	17
18/6/2004	n.a.	3/8/2004	24
19/6/2004	7	4/8/2004	15
20/6/2004	7	5/8/2004	18
21/6/2004	7	6/8/2004	14
22/6/2004	6	7/8/2004	n.a.
23/6/2004	10	8/8/2004	20
24/6/2004	7	9/8/2004	21
25/6/2004	9	10/8/2004	18
26/6/2004	5	11/8/2004	12
27/6/2004	9	12/8/2004	14
28/6/2004	14	13/8/2004	14
29/6/2004	8	14/8/2004	13
30/6/2004	9	15/8/2004	16
1/7/2004	8	16/8/2004	n.a.
2/7/2004	6	17/8/2004	0
3/7/2004	6	18/8/2004	2
4/7/2004	17	19/8/2004	n.a.
5/7/2004	11	20/8/2004	n.a.
6/7/2004	12	21/8/2004	2
7/7/2004	7	22/8/2004	0
8/7/2004	12	23/8/2004	2
9/7/2004	n.a.	24/8/2004	2
10/7/2004	14	25/8/2004	2
11/7/2004	12	26/8/2004	3
12/7/2004	n.a.	27/8/2004	5
13/7/2004	n.a.	28/8/2004	3
14/7/2004	n.a.	29/8/2004	2
15/7/2004	11	30/8/2004	1
16/7/2004	21	31/8/2004	n.a.

TABLE 5. Number of severe scintillations for the period from 1/5/2005 to 31/7/2005 which includes Utah State earthquake of 15/6/2005.

Date	No. of severe scintillations	Date	No. of severe scintillations
1	2	3	4
1/5/2005	n.a.	16/6/2005	13
2/5/2005	1	17/6/2005	12
3/5/2005	1	18/6/2005	13
4/5/2005	2	19/6/2005	12
5/5/2005	4	20/6/2005	14
6/5/2005	5	21/6/2005	15
7/5/2005	8	22/6/2005	13
8/5/2005	4	23/6/2005	14
9/5/2005	3	24/6/2005	10
10/5/2005	7	25/6/2005	13
11/5/2005	5	26/6/2005	11
12/5/2005	3	27/6/2005	9
13/5/2005	3	28/6/2005	13
14/5/2005	5	29/6/2005	12
15/5/2005	4	30/6/2005	14
16/5/2005	2	1/7/2005	11
17/5/2005	4	2/7/2005	14
18/5/2005	3	3/7/2005	18
19/5/2005	4	4/7/2005	13
20/5/2005	4	5/7/2005	14
21/5/2005	6	6/7/2005	12
22/5/2005	6	7/7/2005	5
23/5/2005	9	8/7/2005	9
24/5/2005	10	9/7/2005	9
25/5/2005	11	10/7/2005	7
26/5/2005	10	11/7/2005	8
27/5/2005	17	12/7/2005	13
28/5/2005	15	13/7/2005	14
29/5/2005	13	14/7/2005	18
30/5/2005	10	15/7/2005	9
31/5/2005	6	16/7/2005	7
1/6/2005	n.a.	17/7/2005	4
2/6/2005	n.a.	18/7/2005	4
3/6/2005	13	19/7/2005	9
4/6/2005	17	20/7/2005	4
5/6/2005	16	21/7/2005	3
6/6/2005	15	22/7/2005	5
7/6/2005	13	23/7/2005	6
8/6/2005	n.a.	24/7/2005	10
9/6/2005	16	25/7/2005	9
10/6/2005	13	26/7/2005	5
11/6/2005	10	27/7/2005	6
12/6/2005	10	28/7/2005	7
13/6/2005	11	29/7/2005	7
14/6/2005	11	30/7/2005	8
15/6/2005	11	31/7/2005	n.a.

Discussion

The ionosphere is not strictly uniform, but contains irregularities of different sizes. The effects of these irregularities on propagation of radio waves may be treated by the diffraction theory. As a wave travels through

an irregular medium, it will accumulate changes of amplitude and phase. According to Huygens's principle, each part of the wave front may be regarded as a source of secondary wavelets, the superposition of which builds up the wave front at a point

further along. In diffraction theory, one applies this principle to determine how the amplitude and phase of a received signal are affected by passing through a region of irregularity.

Most scintillations arise in the F region of the ionosphere, although they are also found in the E and D regions. The intensity of scintillation is quantified by means of S_4 index.

The theoretical formula for S_4 index is given in reference [13]. One may omit from the theoretical formula parameters that are either constants or unchanged during observations. We can say that S_4 index is a function of electron density of ionosphere plasma, $S_4 = f(N_e)$. Therefore, the main variable that can affect the scintillation index is the electron density (see [13] for more details).

The motion of electrons in the ionosphere is controlled by the earth magnetic field. Therefore, any variation of geomagnetic field may stimulate variation of electron density.

Thermally driven convection in the Earth's core bends and twists magnetic field lines leading to electric current and large magnetic fields.

Conclusion

The results of this work indicate that there is a tight correlation between the occurrence of a strong earthquake and ionosphere scintillation.

The S_4 index can be a promising factor in predicting earthquakes. This is due to the fact that there is an obvious increase in the S_4 index up to two weeks preceding an earthquake.

Natural radio sources, like radio-galaxies and quasars, can be used to monitor and analyze ionosphere scintillations, instead of GPS satellites. For this propose, it will be enough to locate small radio telescopes (e.g. 10 m diameter) in seismically active regions and perform real time monitoring.

References

- [1]Pulinets, S.A., ASR. 37 (2006) 643.
- [2]Pulinets, S.A., Legen'ka, A.D., Gaivoronskaya, T.V. and Depuev, V.Kh., JASTP. 65 (2003) 1337.
- [3]Pulinets, S.A., Kotsarenko, A.N., Cariole, L. and Pulinets, I.A., ASR. 39 (2007) 970.
- [4]Dabas, R.S., Das Rupesh, M., Sharma, K. and Pillai, K.G.M., JASTP. 69 (2007) 1813.
- [5]Singh, B., Kushwah, V., Singh, O.P., Lakshmi, D.R. and Reddy, B.M., PCE. 29 (2004) 537.
- [6]Sorokin, V.M., Chmyrev, V.M. and Yaschenko, A.K., JASTP. 65 (2003) 21.
- [7]Rothkaehl, H., Bucik, R. and Kudela, K., PCE. 31 (2006) 473.
- [8]Sgringa, V., Buzzia, A., Contia, L., Picozzab, P., Stagnia, C. and Zilpimiani, D., Tectonophys. 431 (2007) 153.
- [9]Dobrovolsky, I.R., Zubkov, S.I. and Myachkin, V.I., Pure and Applied Geophysics, 117 (1979) 1025.
- [10]http://neic.usgs.gov/neis/epic_circ.html.
- [11]<http://stdb2.stelab.nagoya-u.ac.jp/QL-S4/data.html>
- [12]<http://www.spacenv.com/~rice/BLO/s4/S4/index.html>
- [13]Fang, D.J. and Liu, C.H., Radio Sci., 19 (1984) 345.

Jordan Journal of Physics

ARTICLE

Beryllium Doped *p*-type GaN Grown by Metal-Organic Chemical Vapor Deposition

T. M. Al Tahtamouni^a, A. Sedhain^b, J. Y. Lin^b and H. X. Jiang^b

^a*Department of Physics, Yarmouk University, Irbid 21163, Jordan.*

^b*Department of Electrical and Computer Engineering, Texas Tech. University, Lubbock, Texas 79409, USA.*

Received on: 27/6/2010; Accepted on: 21/10/2010

Abstract: The authors report on the growth of Be-doped *p*-type GaN epilayers by metal-organic chemical vapor deposition (MOCVD). The electrical and optical properties of the Be-doped GaN epilayers were studied by Hall-effect measurements and photoluminescence (PL) spectroscopy. The PL spectra of Be-doped GaN epilayers exhibited two emission lines at 3.36 and 2.71 eV, which were absent in undoped epilayers. The transition at 3.36 eV was assigned to the transition of free electrons to the neutral Be acceptor, Be⁰. The transition at 2.71 eV was assigned to the transition of electrons bound to deep level donors to the Be⁰ acceptors. Three independent measurements: (a) resistivity vs. temperature, (b) PL peak positions between Be doped and undoped GaN and (c) activation energy of 2.71 eV transition all indicate that the Be energy level is between 120 and 140 meV above the valence band. This is about 20-40 meV shallower than the Mg energy level (160 meV) in GaN. It is thus concluded that Be could be an excellent acceptor dopant in nitride materials.

Keywords: Be-doped GaN; *p*-type, MOCVD epitaxial growth.

Introduction

Group III nitride semiconductors [1, 2], especially Gallium Nitride (GaN), have successfully been employed to realize blue-green light-emitting diodes, blue laser diodes [3, 4] and ultra violet light sources and detectors [5, 6]. Controllable and efficient doping is one of the most important issues for the development of these devices. For *n*-type doping of nitrides, silicon can be successfully used as dopant and carrier concentrations exceeding (5×10^{20}) cm⁻³ can be achieved [7]. For *p*-type doping, magnesium (Mg) is the acceptor of choice. It can be incorporated in concentrations up to 10²⁰ cm⁻³; however, because of its large ionization energy (~160 meV), the resulting room-temperature hole concentration is only about 10¹⁸ cm⁻³; i.e., only about 1% of Mg atoms are ionized at room temperature. Increasing the Mg concentration beyond 10²⁰ cm⁻³ leads to saturation and a decrease in the hole

concentration [8]. The limited conductivity of *p*-type doped layers impedes progress in device applications. Therefore, it is desirable to find an alternative acceptor. Beryllium has a low theoretical activation energy of about 60 meV [9], making it a promising candidate for *p*-type doping in GaN. In spite of the promising theoretical predictions, practical realization of this idea is very difficult. The main problem with the use of Be as a dopant in GaN is that it is easily incorporated on interstitial sites, where it acts as a donor [10, 11].

Experimentally, Be doping of GaN in molecular beam epitaxy has been reported by various groups [12, 13]. Another technique for Be incorporation that has been attempted is ion implantation [14, 15]. Characterization was mostly by optical spectroscopy measurement. A photoluminescence (PL)

peak just below the band edge of GaN was observed and attributed to Be related transition. Assuming that this PL line results from a Be acceptor, an acceptor energy level can be extracted. However, these results in a wide range of values, ranging from 90 to 250 meV, depending on the assumptions made in the analysis [16]. To the best of our knowledge, there have not been any reports on the growth of Be doped GaN using MOCVD.

Experiment

Be doped GaN epilayers were grown on the c-plane (001) of Al₂O₃ substrates by MOCVD. The growth temperature and pressure were 1080 °C and 70 Torr, respectively. Trimethylgallium (TMGa) and blue ammonia were used as sources for gallium and nitrogen. C₁₀H₁₄O₄Be was used as the Be source. A 2 μm insulating undoped GaN epilayer was grown to serve as a template, followed by the growth of a 0.5 μm Be doped GaN epilayer. X-ray diffraction (XRD) was used to determine crystalline quality, while atomic force microscopy (AFM) was used to study the surface morphology. Variable temperature Hall effect measurement (Standard Van der Pauw) was utilized to assess the electrical properties and PL spectroscopy was employed to investigate the optical properties. The deep UV PL spectroscopy system consists of a frequency quadrupled 100 femtosecond Ti: Sapphire laser with an average power of 3 mW, a repetition rate of 76 MHz at 196 nm and a 1.3 m monochromator with a detection capability ranging from 185 to 800 nm [17].

Results and Discussion

The surface morphology of the Be doped GaN epilayers is relatively rough with a root mean square (RMS) surface roughness of about 6 nm for a 10 μm x 10 μm area, in contrast to the smooth surface of undoped GaN epilayers which have an RMS value of less than 1.5 nm. The (002) peak of Be doped GaN epilayers has a rocking curve full width at half maximum of about 450 arcsec. As grown Be doped GaN epilayers were highly resistive, post growth rapid thermal annealing was done to activate Be acceptors. The annealing conditions were the same as those for Mg acceptor activation (920 °C for 12

seconds under N₂ ambient). Ni/Au was used to make ohmic contacts in the standard Van der Pauw configuration for Hall-effect measurements. Fig. 1 shows the Be and oxygen concentration profiles as measured by secondary ion mass spectrometry (SIMS) for the sample with Be source flow rate of 175 ml/min. The result indicates a Be dopant concentration of about 2 x 10¹⁹ cm⁻³ in the epilayer. The Be dopant concentration was on the order of 10²⁰ cm⁻³ as determined by linear extrapolation from samples measured by SIMS. Oxygen concentration was in the order of 10¹⁸ cm⁻³ and has a negative effect on the material quality and surface morphology. Hall effect measurements indicate the formation of a p-type GaN epilayer by Be doping. The resistivity obtained at room temperature is about 3.7 Ω.cm. Variable temperature Hall-effect measurements were attempted to probe the electrical properties of Be doped GaN epilayers. Fig. 2 shows the Arrhenius plot of the resistivity (ρ) of Be doped GaN epilayers. The resistivity decreases with increasing temperature from 3.7 Ω.cm at 300 K to 2.7 Ω.cm at 600 K. The solid line is the least squares fit of data to the following equation:

$$\rho(T) = \rho_0 [1 + e^{(-E_A/kT)}]^{-1} \quad (1)$$

where ρ(T) is the resistivity at temperature T, E_A is the activation energy and k is the Boltzman constant. The fitted value of the activation energy (E_A) is 118 ± 4 meV.

The average values of hole concentration and mobility at room temperature are ~ 1.7 x 10¹⁸ cm⁻³ and 1.3 cm²/V.s, respectively. The measured values of hole concentration and mobility were fluctuating, so we were not able to use the hole concentration to directly evaluate the activation energy. This fluctuation could be related to the relatively high resistivity of the materials and the unoptimized annealing conditions of the materials and the contacts. More studies are needed to optimize material and annealing conditions for materials and contacts. The small reduction in resistivity between 300 K and 600 K indicates that the materials are highly compensated. This compensation could be due to oxygen molecules in the Be source.

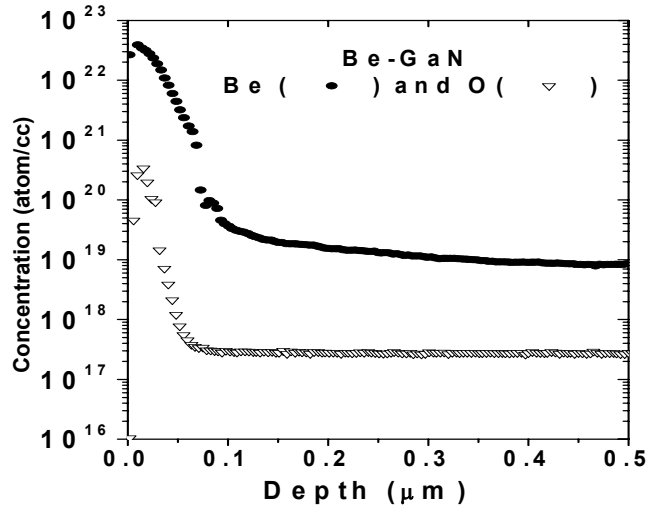


FIG. 1. Oxygen and beryllium dopant concentration profiles in GaN epilayer with Be source flow rate of 175 ml/min, as probed by SIMS (performed by Charles Evans and Associate).

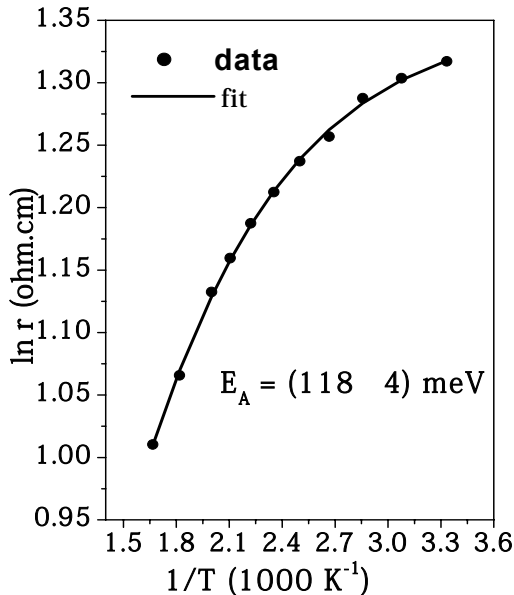


FIG. 2. The Arrhenius plot of resistivity (ρ) between 300 and 600 K for the Be doped GaN epilayers. The solid line is the least-square fit of data with Eq. (1). The fitted value of the activation energy (E_A) for Be is $118 \pm 4 \text{ meV}$.

Low temperature (10 K) PL spectra of Be-doped and undoped GaN epilayers are shown in Fig. 3. The PL spectrum of undoped GaN exhibits a strong band-edge emission at 3.48 eV due to the donor bound exciton (I_2) transition [18]. The band gap of GaN at 10 K is around 3.505 eV [18, 19]. The PL spectrum of Be-doped GaN comprises a band-edge transition at 3.36 eV, which is assigned to the transition of free electrons to neutral Be acceptors (Be^0). A peak at 3.35 eV was observed in Be implanted GaN and assigned

to the transition of the same free electrons to neutral Be^0 recombination [20]. Our assignment determines the energy level of Be acceptors in GaN to be $E_A \sim 3.505 \text{ eV} - 3.36 \text{ eV} = 0.145 \text{ eV}$, which agrees with the value estimated from the temperature dependence of resistivity discussed above. An additional Be related emission line at 2.71 eV was also observed and is believed to be a donor-acceptor-pair (DAP) transition involving deep level donor and Be acceptor. The broad width of the 2.71 eV emission line is a typical characteristic of DAP transitions involving deep level impurity.

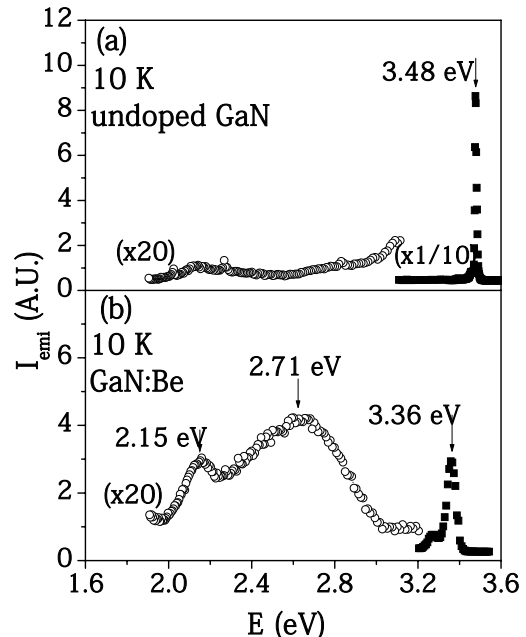


FIG. 3. PL spectra of (a) undoped and (b) Be-doped GaN epilayers measured at 10 K.

Fig. 4 shows the temperature dependence of the 2.71 eV emission line in the Be-doped GaN epilayer measured from 10 to 240 K. The thermal quenching of the 2.71 eV transition is due to the dissociation of the neutral Be acceptor, which is shallower than the energy level of the donor involved. Fig. 5 shows the Arrhenius plot of the 2.71 eV emission intensity in Be-doped GaN. The solid line is the least-squares fit of the data with the equation:

$$I_{emi}(T) = I_0 [1 + Ce^{(-E_0/kT)}]^{-1} \quad (2)$$

where $I_{emi}(T)$ and I_0 are the integrated PL intensity at temperature T and 0 K and E_0 is the activation energy of PL emission intensity. The fitted value of the activation energy E_0 is 126 meV. This value is close to the activation energy determined from the temperature dependent resistivity measurement. All these results indicate that the energy level of Be is between 120 and 145 meV and is about 20-40 meV shallower than that of Mg in GaN.

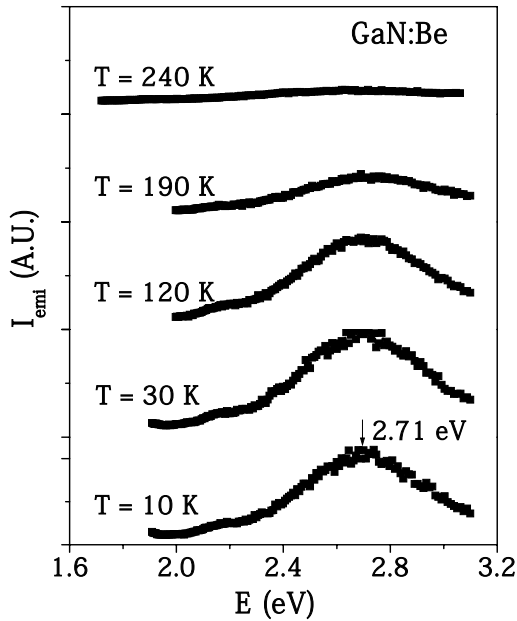


FIG. 4. PL spectra of 2.71 eV emission line of Be-doped GaN epilayer measured between 10 and 240 K.

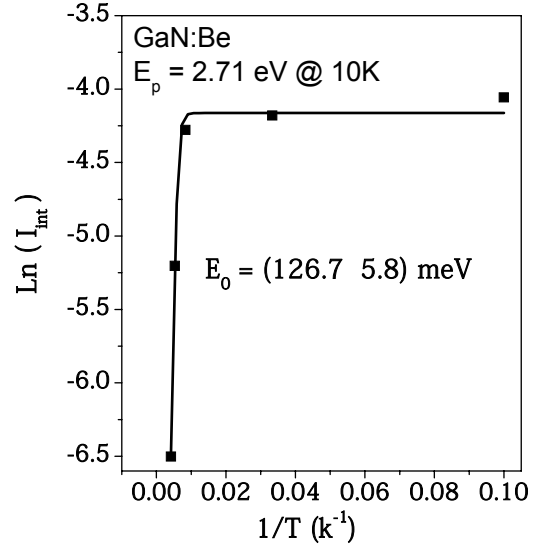


FIG. 5. The Arrhenius plot of the integrated PL emission intensity of the 2.71 eV emission line in Be-doped GaN. The solid line is the least-squares fit of data with Eq. (2). The fitted value of the activation energy (E_0) of Be acceptor is 126.7 ± 5.8 meV.

Conclusion

Be-doped GaN epilayers were grown by MOCVD and their optical and electrical properties were probed. It was confirmed from Hall measurement that these epilayers are p -type. The activation energy of Be acceptors was deduced to be between 120 and 145 meV from Hall-effect measurement, direct comparison of band-edge transitions and activation energy of DAP transition. The energy level of Be is about 20-40 meV shallower than the Mg level in GaN. These results thus suggest that Be could be an excellent candidate as a p -type dopant in GaN. Additional improvements in material quality, doping conditions and annealing parameters of materials and contacts would further enhance the material conductivity.

References

- [1] Strite, S. and Morkoc, H., *J. Vac. Sci. Technol. B*, 10 (1992) 1237.
- [2] Morkoc, H., Strite, S., Gao, G.B., Lin, M.E., Sverdlov, B. and Burns, M., *J. Appl. Phys.* 76 (1994) 1363.
- [3] Pearton, S.J., Vartuli, C.B., Zolper, J.C., Yuan, C. and Stall, R.A., *Appl. Phys. Lett.* 67 (1995) 1435.
- [4] Nakamura, S. and Fasol, G., *The Blue Laser Diode-Gallium-Nitride Based Light Emitters and Laser*, (Springer, Berlin, 1997).
- [5] Goldenberg, B., Zook, J.D. and Ulmer, R.J., *Appl. Phys. Lett.* 62 (1993) 381.
- [6] Walker, D., Saxler, A., Kung, P., Zhang, X., Hamilton, M., Daiz, J. and Razeghi, M., *Appl. Phys. Lett.* 72 (1998) 3303.
- [7] Gotz, W., Kern, R.S., Chen, C.H., Liu, H., Steigerwald, D.A. and Fletcher, R.M., *Mater. Sci. Eng., B*, 59 (1999) 211.
- [8] Bour, D.P., Chung, H.F., Gtz, W., Romano, L., Krusor, B.S., Hofstetter, D., Rudaz, S., Kuo, C.P., Ponce, F.A., Johnson, N.M., Craford, M.G. and Bringans, R.D., in "III-V Nitrides", edited by F.A. Ponce, T.D. Moustakas, I. Akasaki and B. Monemar, *MRS. Symp. Proc. No. 449*, p. 509 (MRS, Pittsburgh, 1997).
- [9] Bernardini, F., Fiorentini, V. and Bosin, A., *Appl. Phys. Lett.* 70 (1997) 2990.
- [10] Neugebauer, J. and Van de Walle, G., *J. Appl. Phys.* 85 (1999) 3003.
- [11] Teisseyre, H., Gorczyca, I., Christensen, N.E., Svane, A., Naranjo, F.B. and Calleja, E., *J. Appl. Phys.* 97 (2005) 043704.
- [12] Salvador, A., Kim, W., Aktas, O., Botchkarev, A., Fan, Z. and Morkoc, H., *Appl. Phys. Lett.* 69 (1996) 2692.
- [13] Cheng, T., Hooper, S., Jenkins, L., Foxon, C., Lacklison, D., Dewsnip, J. and Orton, J., *J. Cryst. Growth*, 166 (1996) 597.
- [14] Ronning, C., Carlson, E., Thomson, D. and Davis, R., *Appl. Phys. Lett.* 73 (1998) 1622.
- [15] Ronning, C., Linthicum, K., Carlson, E., Hartlieb, P., Thomson, D., Gehrke, T. and Davis, R., *MRS Internet J. Nitride Semicond. Res.* 4S1 (1999) G3.17.
- [16] Van de Walle, G., Limpijumngong, S. and Neugebauer, J., *Phys. Rev. B*, 63 (2001) 245205.
- [17] <http://www2.ece.ttu.edu/nanophotonics>
- [18] Chen, G.D., Smith, M., Lin, J.Y., Jiang, H.X., Wei, S.H., Asif Khan, M. and Sun, C.J., *Appl. Phys. Lett.* 68 (1996) 2784.
- [19] Smith, M., Chen, G.D., Lin, J.Y., Jiang, H.X., Salvador, A., Kim, W.K., Aktas, O., Botchkarev, A. and Morkoc, H., *Appl. Phys. Lett.* 67 (1995) 3387.
- [20] Ronning, C., Carlson, E.P., Thomson, D.B. and Davis, R.F., *Appl. Phys. Lett.* 73 (1998) 1622.

Jordan Journal of Physics

ARTICLE

Visibility Degradation and Light Scattering/Absorption Due to Aerosol Particles in Urban/Suburban Atmosphere of Irbid, Jordan

Khadeejeh M. Hamasha^{a+b}

^a*Department of Physics, Yarmouk University, Irbid, Jordan.*

^b*Department of Physics, University of Tabuk, Saudi Arabia.*

Received on: 17/05/2010; Accepted on: 31/10/2010

Abstract: Visible light scattering and absorption patterns were measured using a photoacoustic instrument at different locations in Irbid city. Measurements were performed during the intervals 1 – 9 August 2007 and 7 – 13 October 2007 at the city center site (Palestine Street) and the southern site (University Circle), respectively. The city center site is impacted by local urban and regional aerosols. The southern site is dominated by regional aerosols. Data from both sampling sites showed variety of diurnal light absorption and scattering patterns. During most of the measurement days, the highest light absorption peaks appeared in the morning, 7:00 – 9:30 AM, whereas the highest light scattering peaks appeared later, 9:30 – 11:00 AM. The earlier light absorption peaks are likely attributed to the elevated black carbon vehicular emission during the heavy traffic hours (rush hours) whereas, the later light scattering peaks are attributed to secondary aerosols generated in the atmosphere through photochemical reactions. The southern site (University Circle) exhibited a higher light scattering and a lower light absorption contribution to the light extinction, leading to a better visibility compared to the City Center site. The visibility is averaged at 44 km and 115 km at the city center site and the southern site, respectively.

Keywords: Light absorption; Light scattering; Light extinction; Visibility.

Introduction

Visibility is defined as the greatest distance at which an observer can just see a black object viewed against the horizon [1]. An object is usually referred to as the threshold contrast when the difference between the brightness of the sky and the brightness of the object is reduced to such a degree that an observer can just barely see the object. Much effort has been expended in establishing the threshold contrast for various targets under a variety of illumination and atmospheric conditions [2]. Nevertheless, visibility is more than being able to see a black object at a distance for which the contrast reaches a threshold value. Visibility is more closely associated with the conditions that allow the appreciation of inherent beauty of landscape features. It is important to recognize and appreciate the form, contrast, detail and color of near and distance features.

It is necessary to understand what constituents in the atmosphere reduce visibility.

Atmospheric visibility can be reduced by fog, snow, dust, sand, smog or any combination of these and is a part of normal atmospheric phenomena. The loss of visibility that commonly accompanies high pollutant levels is perhaps the aspect of air pollution most obvious to the public. It is due to scattering and absorption of light by pollutants [1]. The total light extinction (the sum of scattering and absorption by gases and particles) and hence visibility reduction depends on both wavelength of the light and scattering angle, that is the position of the sun, so the haze due to air pollution may appear to have different colors and densities, depending on the condition.

In spite of the fast growth of urban areas and industrial activities in Jordan, air pollution has not yet received due attention. Air quality is not routinely monitored anywhere, except at Alhashameiah (located in the Zarqa governorate to the northeast of Zarqa city) which experiences high levels of sulfur oxides and particulates. There have been a few studies that tackled air pollution in Jordan by aerosol particles. Hamasha *et al.* (2010) [3] reported the levels of black carbon at several urban and industrial locations in Jordan during summer of 2007 and winter of 2008. Another study was carried out by Hamasha and Arnott (2009) [4] on the black carbon light absorption coefficients in Irbid city. They found that the average B_{ap} in Irbid was 41.4 Mm^{-1} .

Irbid is Jordan's third largest city. Its population amounts to 255083 people According to the 2004 census [5]. It is situated on a plain land with an area of 36.9 km^2 , and it is 100 km to the north of the capital, Amman. Irbid city is seated in a highland plateau, 620 meters above sea level. It is also close to three neighboring states, and there are no natural barriers to prevent pollution transport in the region. In fact, Irbid is less than 70 km to the east of Haifa, 120 km south-east of Beirut and 80 km south of Damascus, and most of the wind blows from the west and the north. This means that Irbid is downwind from anthropogenic activities in the east Mediterranean coast. Therefore, it is an ideal town to study regional impact of air pollution.

The purpose of this manuscript was to study the diurnal aerosol visible light absorption and scattering during the intervals 1 – 9 August 2007 and 7 – 13 October 2007 at the city center site (Palestine Street) and the southern site (University Circle), respectively, and to determine the aerosols impact on the visibility degradation and its variation from the city center site (urban) and the southern site (suburban) in Irbid through the measurement and analysis of the time series of black carbon light absorption and scattering coefficients.

Light Scattering and Absorption

Solar radiation passing through the atmosphere to the earth surface is both

scattered and absorbed by gases and particles. The intensity of radiation striking the surface can be expressed in the form of Beer-Lambert law:

$$I = I_0 e^{-B_{ext} L} \quad (1)$$

where I_0 and I are the incident and transmitted light intensities, respectively, L is the path length of the light beam and B_{ext} is the light extinction coefficient with the unit of $(\text{length})^{-1}$. This extinction coefficient, representing the total reduction in the light intensity due to scattering and absorption of light by gases and particles, is the sum of two terms,

$$B_{ext} = B_{extg} + B_{extp} \quad (2)$$

where B_{extg} is the extinction due to the gases and B_{extp} is the extinction due to the particles. Each of these terms can be broken down into contributions from light scattering and absorption so that equation (2) becomes:

$$B_{ext} = B_{ag} + B_{sg} + B_{ap} + B_{sp} \quad (3)$$

where B_{ag} and B_{sg} are the light extinctions due to absorption and scattering by gases and B_{ap} and B_{sp} are those due to absorption and scattering by particles. The gaseous contributions to the light extinction in the visible region are generally small [6 – 9]. Gas absorption in the visible region is limited to NO_2 . However, light absorption by NO_2 is usually much less than the total light extinction by particles. Thus, when NO_2 is present in sufficient concentrations to absorb light, the atmosphere usually contains relatively high concentrations of other pollutants, including particles. As a result, light scattering and absorption by particles usually exceed light absorption by NO_2 [6, 10, 11]. Gas scattering is essentially equal to Rayleigh scattering due to molecular oxygen and nitrogen and has relevance only in rural areas where the total extinction is small.

The degree at which aerosol light absorption contributes to the total aerosol light extinction, G_{ap} , and the contribution of the aerosol light scattering to the total aerosol light extinction or single scattering albedo, ω , are determined, respectively, as:

$$G_{ap} = \frac{B_{ap}}{B_{extp}} \quad (4)$$

$$\omega = \frac{B_{sp}}{B_{extp}} \quad (5)$$

Relationship of Light Scattering and Absorption to Visibility Reduction

One of the most evident manifestations of anthropogenic air pollution is the production of haze which causes a reduction in visibility; that is, in visual range. Two factors enter into visual range: visual acuity and contrast. In day time, atmosphere particles reduce the contrast perceived by an observer by scattering light from the object out of the line of sight to the observer's eyes. Simultaneously, sunlight is scattered into the line sight, making dark objects appear lighter. The result is a decrease in the contrast between the object and the horizon. At night, scattering of light out of the visual path decreases the contrast and hence the source intensity becomes a factor in visual range as well.

The Koschmieder equation has been shown to approximate the change in contrast of an object with distance away from an observer [12]. According to Koschmieder equation, visibility, Vis , is defined as:

$$Vis = \frac{Ln(C_0/C)}{B_{ext}} \quad (6)$$

where C_0 is the contrast relative to the horizon (or background) of an object seen at the observation point itself; that is at a distance $L = 0$ and C is the contrast at distance L . The contrast is defined as the ratio of the brightness of the object (B_0) to the brightness of the horizon or background (B_H), minus one:

$$C = \frac{B_0}{B_H} - 1 \quad (7)$$

Observers typically can differentiate objects on the horizon if $C/C_0 \sim 0.02 - 0.05$. A contrast of 0.02 corresponds to a visual range of

$$Vis = \frac{Ln(C_0/C)}{B_{ext}} = \frac{3.912}{B_{ext}} \quad (8)$$

Measurements

In this study, diurnal aerosol light absorption and scattering coefficients were obtained using the photoacoustic instrument

at a wavelength of 870 nm for two sites in Irbid city/Jordan. The first period was 1 – 9 August 2007 at the city center close to Palestine Street; a very crowded main street with heavy duty diesel buses and automobiles. This site is a highly populated region, having many stores and is crowded with large buildings that give rise to urban canyon effects on wind flow. The second period was from 7 - 13 October 2007 in the south of the city near the north gate of Yarmouk University (University Circle). The degree at which aerosol scattering and absorption contribute to the total aerosol light extinction is further determined and the aerosol impact on aerosol visibility degradation and its variation is quantified.

Light absorption and scattering coefficients at a wavelength of 870 nm were recorded with the photoacoustic instrument [13]. The photoacoustic instrument utilizes a microphone to record sound issuing from heat transferred from light absorbing aerosols to the surrounding air. A power meter records the laser power. The ratio of microphone pressure and laser power is used to obtain the light absorption coefficients. The photoacoustic instrument measures aerosol light absorption and scattering coefficient (B_{ap} , B_{sp}) directly for airborne particulate matter. It provides an absorption measurement that can be compared to the more commonly used Particle Soot Absorption Photometer (PSAP) and Aethalometer, but it is without the filter-based artifacts and resulting correction factors. An evaluation mechanism for calibration of light absorption by the photoacoustic instrument exists in employing light-absorbing gases such as nitrogen dioxide [14]. The large dynamic range of measurement provides another advantage for photoacoustic measurements. Finally, inclusion of scattering measurement along with light absorption within a single instrument allows for the calculation of extinction and single scattering albedo, the most important parameters in aerosol radiative forcing and atmospheric visibility.

Light scattering by aerosols is measured in the photoacoustic instrument by the method of reciprocal nephelometry [15]. In a reciprocal integrating nephelometer arrangement, a parallel beam of light is used

to illuminate a scattering volume, and scattered light is detected by a cosine-weighted detector so that the measured optical power is proportional to the total scattering cross section [16]. Within the instrument, the laser beam provides the parallel light source and the cosine-weighted detector is positioned on the resonator to view the center of the sample cavity. The cosine-weighted sensor is fiber coupled to the photomultiplier tube (PMT).

The coefficient of scattering B_{sp} is calculated using the magnitude of the Fourier transformed functions of PMT signal and laser power at resonance frequency. The expression for determining B_{sp} is given by:

$$B_{sp} = \alpha \frac{|\tilde{P}_{PMT}|}{|\tilde{P}_L|}, \quad (9)$$

where α is the calibration factor determined during instrument calibration. The photomultiplier tube signal is given by P_{PMT} and P_L is the measured laser power. The magnitudes of these two complex functions of frequency are used in equation (9). Background measurements of scattering are also periodically made during instrument operation of light scattering by filtered air within the resonator. The scattering background is subtracted from the PMT signal to produce the reported coefficient of scattering.

The experimental procedure is to setup the photoacoustic instrument in a well-ventilated area where the air could be brought in. The instrument is controlled by a Labview program. When it is ready to sample air, the instrument inlet flexible tubing is connected to the inlet of copper tubing so that the air sample can be pulled in. This copper tubing was fixed to some stable wall with its inlet open all the time during sampling. A pump was used to draw outside the air through the instrument with a volume flow rate of 31 min^{-1} . The light absorption and scattering measurements were performed approximately every two minutes during the observational periods.

Results and Discussion

A survey of the average diurnal aerosol visible light absorption and scattering

coefficients (Tables 1 and 2) revealed that the average daily aerosol B_{ap} had maximum values of 69 Mm^{-1} and 12 Mm^{-1} and minimum values of 16 Mm^{-1} and 1 Mm^{-1} for the city center site and the southern site, respectively. The average values for two periods in the city center site and the southern site, respectively, were 39 Mm^{-1} and 7 Mm^{-1} . The average values for the whole two periods of the daily aerosol B_{sp} for the city center site and the southern site, respectively, were 77 Mm^{-1} and 62 Mm^{-1} with maximum values of 132 Mm^{-1} and 114 Mm^{-1} and minimum values of 39 Mm^{-1} and 30 Mm^{-1} . The aerosol light extinction coefficients values were calculated from the absorption and scattering coefficients. The calculated black carbon (BC) using the absorption coefficients shows minimum values on Friday during the two measurement periods, which is expected as Friday is a non-working day in Jordan. In general, B_{ap} and B_{sp} values vary significantly throughout the measurement days (Figs. 1 and 2). B_{ap} and B_{sp} values were higher in the morning than in the afternoon, with several incidences where B_{ap} exceeded the B_{sp} in the early morning (Fig. 3). For most of the measurement days, the highest absorption peaks appeared in the early morning, 7:00 – 9:30 AM. While those of the scattering appeared later, 9:30 – 11:00 AM. The earlier absorption peaks could be attributed to the elevated black carbon emissions during the heavy traffic hours whereas, the later scattering peaks could be attributed to secondary aerosols formed through photochemical reactions in the atmosphere. The average values of B_{ap} and B_{sp} at the city center site were large and comparable to urban residential areas in large cities like Granada, Spain [17] and Guangzhou, China [18]. Lyamani *et al.* (2010) reported average values of B_{ap} (21 Mm^{-1} at 670 nm) and B_{sp} (40 Mm^{-1} at 700 nm, 60 Mm^{-1} at 550 nm, 80 Mm^{-1} at 450 nm) measured in Granada, Spain during the period from 1 December 2005 to 30 November 2007. Andreae *et al.* (2008) reported average values of B_{ap} (91 Mm^{-1} at 450 nm) and B_{sp} (418 Mm^{-1} at 450 nm) measured during the Pearl River Delta measurement campaign in urban Guangzhou, China during the period 4 October 2004 to 5 November 2004.

TABLE 1. Daily average aerosol optical parameters (Mean \pm SD) in Irbid city center site.

Date	B_{ap} (Mm^{-1})	B_{sp} (Mm^{-1})	B_{extp} (Mm^{-1})	ω B_{sp}/B_{extp}	G_{ap} B_{ap}/B_{extp}	Vis (km)	BC ($\mu g/m^3$)
8/1/2007 Wednesday	69 \pm 20	66 \pm 45	135 \pm 64	0.44 \pm 0.14	0.56 \pm 0.14	37 \pm 22	11.3 \pm 3.0
8/2/2007 Thursday	66 \pm 21	42 \pm 21	108 \pm 26	0.38 \pm 0.17	0.62 \pm 0.17	38 \pm 10	10.8 \pm 3.0
8/3/2007 Friday	16 \pm 2	49 \pm 31	65 \pm 32	0.69 \pm 0.16	0.31 \pm 0.16	78 \pm 46	2.6 \pm 0.9
8/4/2007 Saturday	37 \pm 9	39 \pm 20	76 \pm 40	0.51 \pm 0.13	0.49 \pm 0.13	51 \pm 33	6.1 \pm 2.1
8/5/2007 Sunday	25 \pm 9	132 \pm 45	157 \pm 46	0.82 \pm 0.08	0.18 \pm 0.08	29 \pm 14	4.0 \pm 1.9
8/6/2007 Monday	36 \pm 33	90 \pm 75	126 \pm 91	0.68 \pm 0.20	0.31 \pm 0.20	47 \pm 32	5.9 \pm 5.4
8/7/2007 Tuesday	41 \pm 10	94 \pm 90	135 \pm 29	0.62 \pm 0.16	0.38 \pm 0.16	40 \pm 22	7.0 \pm 2.2
8/8/2007 Wednesday	29 \pm 11	54 \pm 20	83 \pm 24	0.65 \pm 0.14	0.35 \pm 0.14	47 \pm 22	4.7 \pm 2.1
8/9/2007 Thursday	32 \pm 17	129 \pm 65	161 \pm 70	0.77 \pm 0.13	0.23 \pm 0.13	31 \pm 19	5.3 \pm 3.1
average	39	77	116	0.65	0.35	44	6.4
Standard deviation	18	36	35	0.16	0.16	15	2.9

TABLE 2. Daily average aerosol optical parameters (Mean \pm SD) in the southern site of Irbid city.

Date	B_{ap} (Mm^{-1})	B_{sp} (Mm^{-1})	B_{extp} (Mm^{-1})	ω B_{sp}/B_{extp}	G_{ap} B_{ap}/B_{extp}	Vis (km)	BC ($\mu g/m^3$)
10/7/2007 Sunday	10 \pm 5	46 \pm 17	57 \pm 20	0.82 \pm 0.12	0.18 \pm 0.12	68 \pm 31	1.7 \pm 0.7
10/8/2007 Monday	6 \pm 6	114 \pm 80	121 \pm 83	0.92 \pm 0.10	0.08 \pm 0.10	81 \pm 107	1.0 \pm 1.0
10/9/2007 Tuesday	8 \pm 4	83 \pm 44	91 \pm 46	0.88 \pm 0.11	0.12 \pm 0.11	68 \pm 66	1.3 \pm 0.6
10/10/2007 Wednesday	9 \pm 23	67 \pm 80	76 \pm 91	0.86 \pm 0.14	0.14 \pm 0.14	114 \pm 88	1.6 \pm 3.7
10/11/2007 Thursday	12 \pm 10	30 \pm 23	42 \pm 27	0.70 \pm 0.21	0.31 \pm 0.23	168 \pm 230	2.0 \pm 1.6
10/12/2007 Friday	1 \pm 2	40 \pm 30	41 \pm 30	0.93 \pm 0.13	0.07 \pm 0.13	202 \pm 260	0.2 \pm 0.3
10/13/2007 Saturday	5 \pm 4	53 \pm 32	59 \pm 31	0.86 \pm 0.18	0.14 \pm 0.18	102 \pm 107	0.9 \pm 0.7
average	7	62	70	0.85	0.15	115	1.2
Standard deviation	4	29	29	0.08	0.08	52	0.6

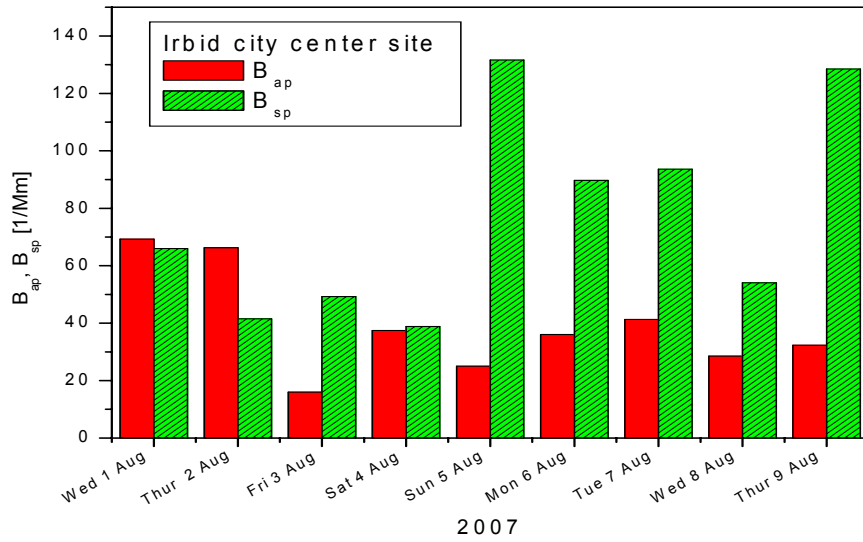


FIG. 1. Daily average aerosol light absorption and scattering coefficients at the city center site of Irbid city for the period 1 – 9 August 2007.

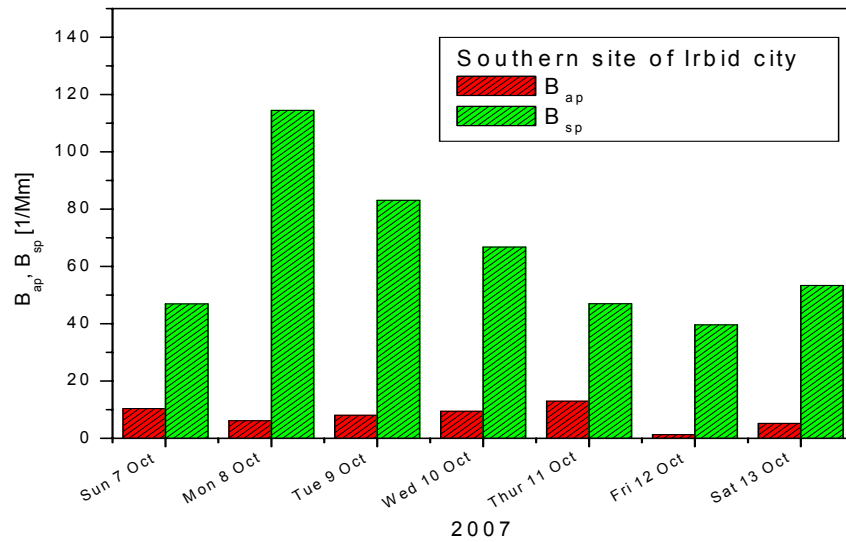


FIG. 2. Daily average aerosol light absorption and scattering coefficients at the southern site of Irbid city for the period 7 – 13 October 2007.

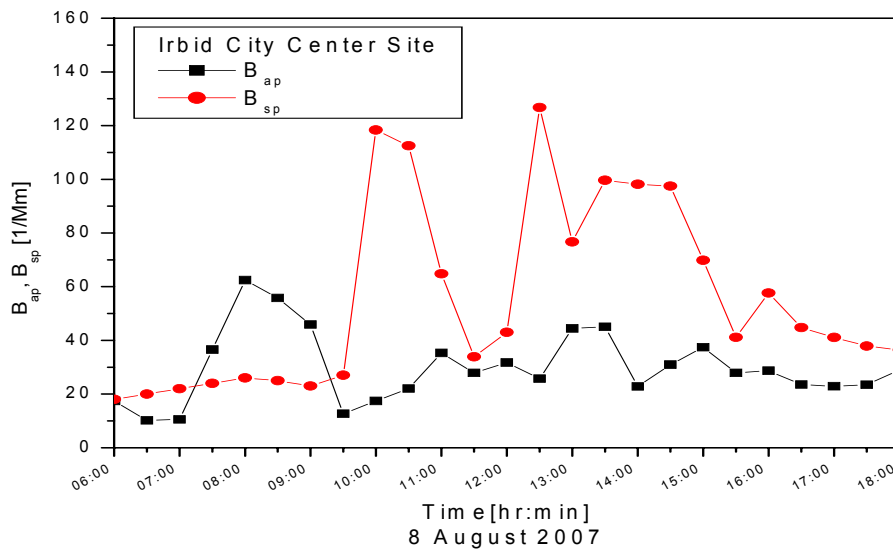


FIG. 3. Diurnal aerosol visible light absorption and scattering pattern on August 8, 2007 in the city center site, where B_{ap} exceeds B_{sp} in the early morning and B_{sp} has its first peak at 10 AM.

The contribution of aerosol light absorption to the total aerosol light extinction, G_{ap} , varied from 0.16 to 0.62 at the city center site and from 0.07 to 0.18 at the southern site. During the study periods, G_{ap} first peak was observed in the early morning (6:30-8:00, Fig. 4). The G_{ap} peaks are understandable considering that light absorption is dominated by BC in the primary vehicle emissions, which is elevated during morning and evening rush hours.

On the other hand, the single scattering albedo, ω (the contribution of the aerosol light scattering to the total aerosol light extinction), varies from 0.38 to 0.84 at the city center site and from 0.70 to 0.93 at the southern site. The ω variability described above was the opposite of G_{ap} variability as expected ($\omega = 1 - G_{ap}$, Fig. 5), reflecting the fact that light scattering, which is dominated by photochemically formed aerosols, is minimal in the morning before the onset of much photochemistry.

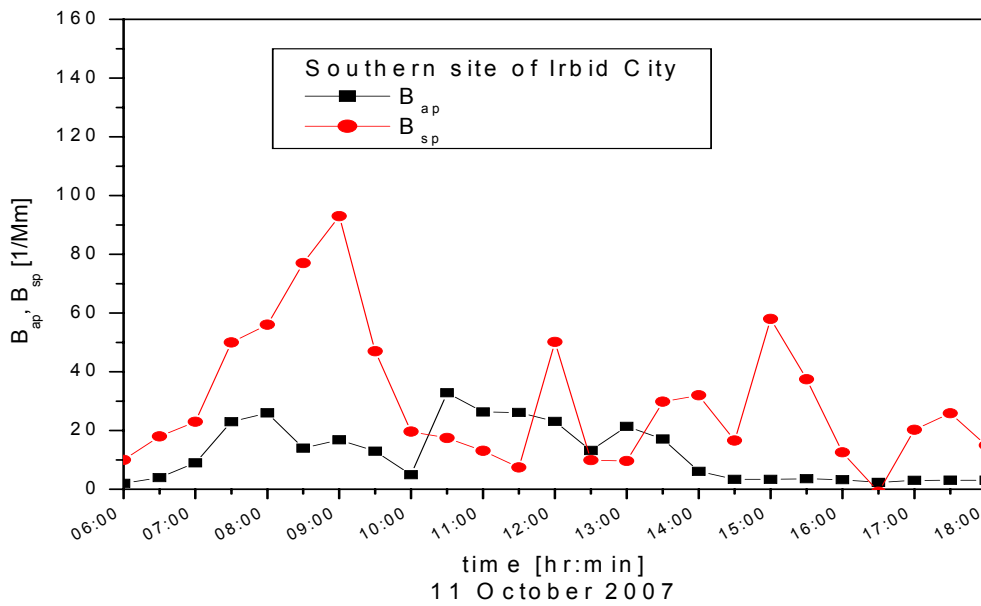


FIG. 4. Diurnal aerosol visible light absorption and scattering pattern on October 11, 2007 in the southern site, where B_{ap} exceeds B_{sp} in the early morning and B_{sp} has its first peak at 9:00 AM.

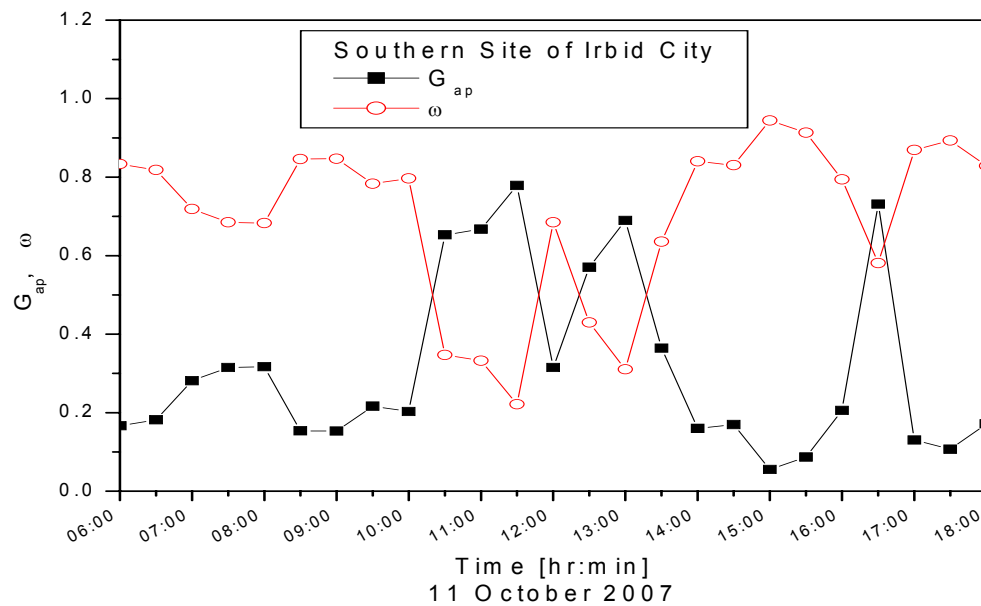


FIG. 5. Variation of G_{ap} and ω parameters during the day of October 11, 2007 at the southern site of Irbid City, where G_{ap} has its first peak at 7:30 AM, while ω has its first peak at 9:00AM.

Visibility due to aerosol, Vis , in turn, varied from 29 km on Sunday, 5 August 2007 to 78 km on Friday, 3 August 2007 at the city center site (Fig. 6) and from 68 km on Sunday, 7 October 2007 to 202 km on Friday, 12 October 2007 at the southern site (Fig. 7). For both sites, the clearest day was Friday. Diurnal aerosol visibility variations for the days that have maximum and minimum observed values during measurement days are shown in Figs. 8 and 9. The overall averages

Vis were 44 km and 115 km for the city center site and southern site, respectively. The city center site visibility is comparable to the average visibility of a polluted city like Mexico City [19], since the city center site is close to Palestine Street, which experiences heavy traffic of all types of vehicles including heavy duty diesel buses and trucks. Furthermore, this site is located in a highly populated region [4].

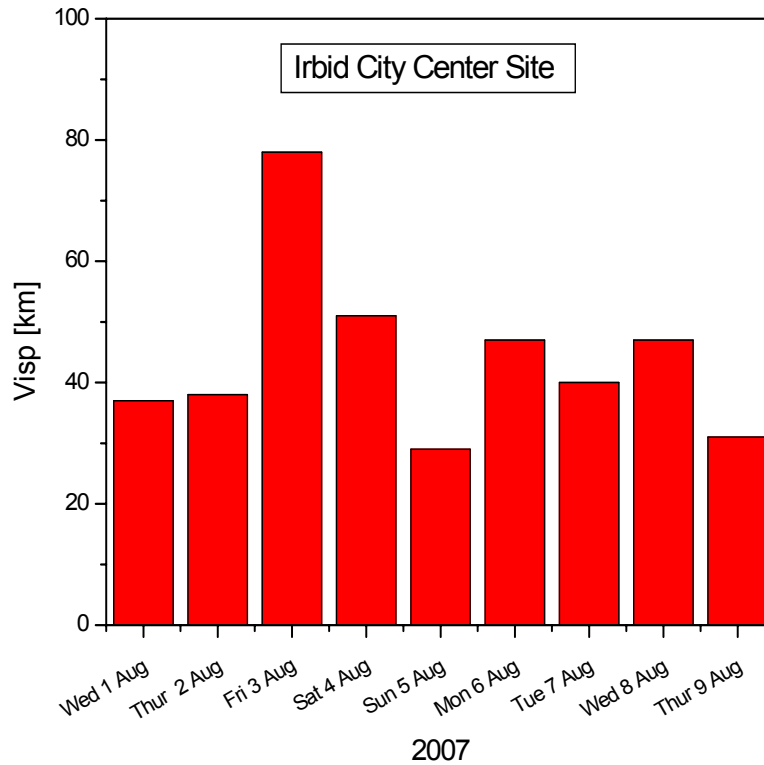


FIG. 6. Daily average visibility at Irbid city center site.

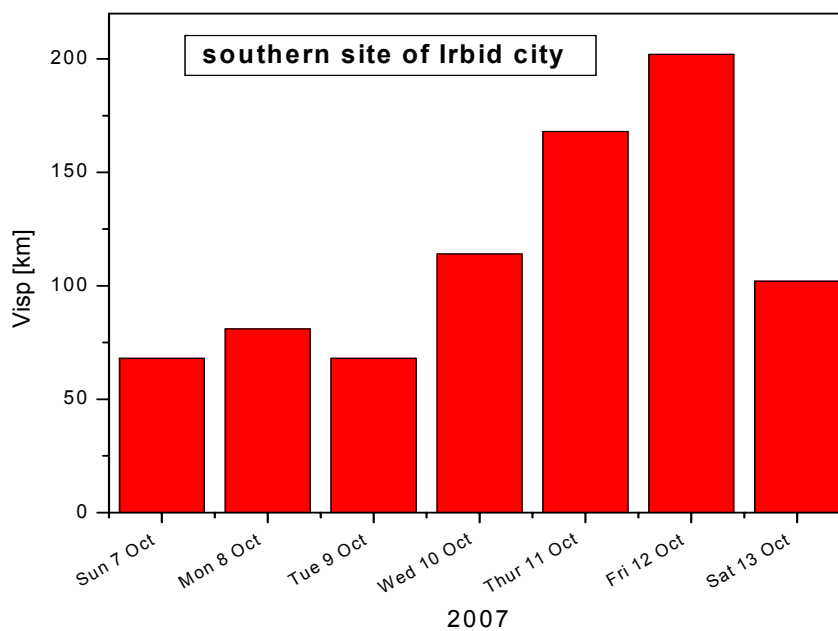


FIG. 7. Daily average visibility at Irbid southern site.

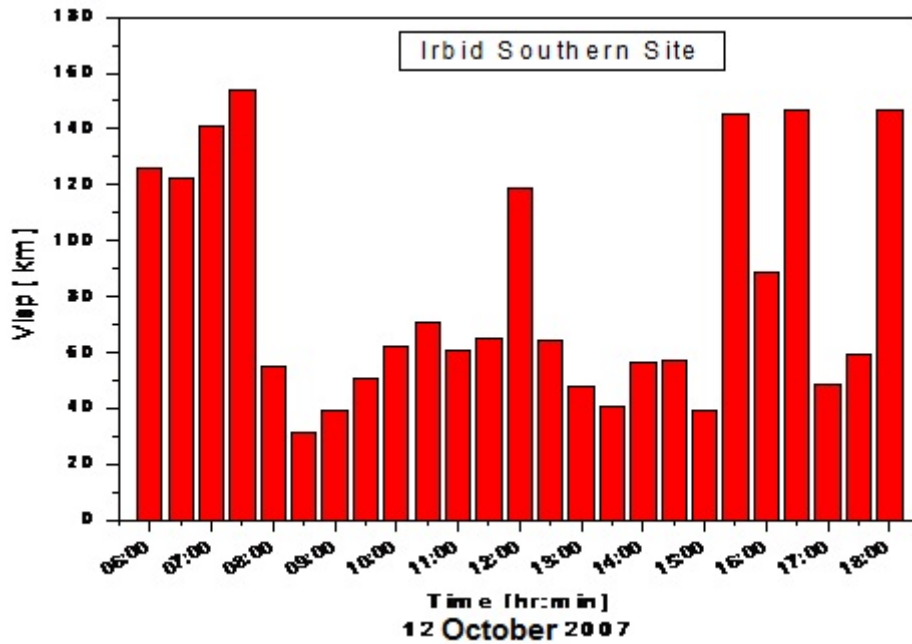


FIG. 8. Diurnal aerosol visibility variation on the day where the maximum value of all the studied days was achieved.

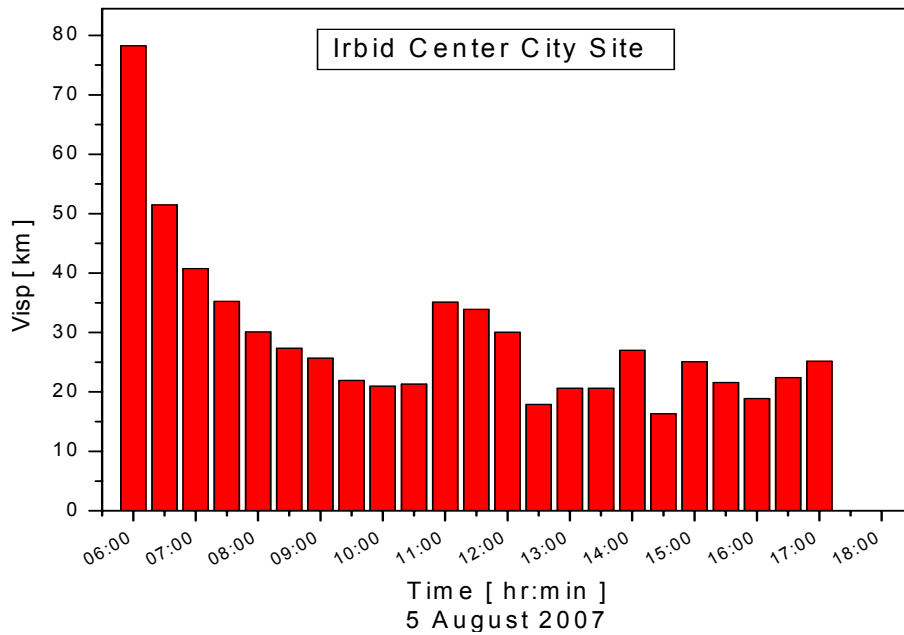


FIG. 9. Diurnal aerosol visibility variation on the day where the minimum value of all the studied days was achieved.

The impact of B_{ap} on visibility can be further illustrated considering the aerosol parameters of two days; 4 and 6 August for which the average black carbon coefficients (BC) were similar. During those days, BC values were 6.1 and 5.9 $\mu\text{g}/\text{m}^3$ ($\text{BC} = B_{ap}/6.11$, for details see Hamasha and Arnott, 2009). According to the average aerosol visibility values given in Table 1, 4 August is

clearer than 6 August. On 4 August, light absorption was responsible on average for 49% of the visibility degradation caused by aerosols. On the hazier day (6 August), aerosol light absorption was responsible on average for only 31% of the visibility degradation caused by aerosols. These results for Irbid city compare well with the published observations reported from Los-Angeles [9]

and Mexico City [19], that aerosol light absorption contribution to aerosol visibility degradation increases under less polluted conditions.

The overall studied days aerosol visibility average of 44 km found at the city center site (affected by regional - as well as by urban-generated aerosols) was 71 km lower than that of 115 km found at the southern site (dominated by regional scale aerosols). This big difference is likely due to the regional influence in addition to the urban influence.

Summary and Conclusion

Diurnal aerosol visible light absorption and scattering coefficients at the wavelength of 870 nm were obtained using the photoacoustic instrument during 1-9 August 2007 at Irbid city center site and during 7-13 October 2007 at Irbid southern site. The diurnal absorption and scattering patterns showed a strong variability from day to day at both sites. During most of the study days, the highest absorption peaks appeared in the early morning, while those of scattering appeared at later times. The earlier absorption peaks could be attributed to the elevated black carbon emissions during the heavy traffic hours whereas, the later scattering

peaks are attributed to secondary aerosols formed photochemically in the atmosphere. During the sampling period, the southern site exhibited on average a higher aerosol scattering and a lower aerosol absorption contribution to the total aerosol visible light extinction and a better visibility than the city center site. The average visibility attributed to aerosols at the city center site dominated by urban scale and regional scale was 44 km, while that at the southern site was 115 km.

Acknowledgements

Photoacoustic instrument was borrowed from the United State of America via an agreement between Yarmouk University/ Deanship of Research and Graduate Studies and Dr. Patrick Arnott from the Physics Department at the University of Nevada/Reno.

The author acknowledges the financial support of the Deanship of Scientific Research and Graduate Studies at Yarmouk University (Grant number 2006/25).

It is a pleasure to thank Dr. Patrick Arnott for his helpful discussion, and Hussam Al-Omari and Mohammad Jaradat for their help in conducting the field measurements.

References

- [1] Finlayson-Pitts, B.J. and Pitts, Jr. J.N., *Chemistry of the Upper and Lower Atmosphere*. (Academic Press, 2000).
- [2] Malm, W.C., *Introduction to Visibility*. CIRA, NPS Visibility Program, (Colorado State University, Front Collin, CO 80523, 1999). ISSN 0737-5352-40.
- [3] Hamasha, K.M., Almomani, M.S., Abu-Allaban, M. and Arnott, W.P., *Jordan Journal of Physics*, 3 (2010) 1.
- [4] Hamasha, K.M. and Arnott, W.P., *Environ. Monit. Assess.* 166 (2009) 485, DOI 10.1007/s10661-009-1017-3.
- [5] Greater Irbid Municipality. Retrieved 16 April 2009 from <http://www.Irbid.gov.jo>.
- [6] Grobliki, P.J., Wolff, G.T. and Countess, R.J., *Atmos. Environ.* 15 (1981) 2473.
- [7] Dzubay, T.G., Stevens, R.K., Lewis, C.W., Hern, D.H., Courtney, W.J., Tesh, J.W. and Mason, M.A., *Environ. Sci. Technol.* 16 (1982) 514.
- [8] Partinis, S., Novakov, T., Ellis, E.C. and Friendlander, S.K., *J. Air Pollut. Control Ass.* 34 (1984) 643.
- [9] Adams, K.M., Davis, L.I. Jr., Japar, S.M. and Finley, D.R., *Atmos. Environ.* 24A (1990) 605.
- [10] Waggoner, A.P., Weiss, R.E. and Ahlquist, N.C., *Atmos. Environ.* 17 (1983) 2081.
- [11] Larson, S.M. and Cass, G.R., *Environ. Sci. Technol.* 23 (1989) 281.
- [12] Middleton, W.E.K., *Vision through the Atmosphere*, (Univ. of Toronto Press, Toronto, 1952).

- [13] Arnott, W.P., Moosmüller, H., Rogers, C.F., Jin, T. and Bruch, R., *Atmospheric Environment*, 33 (1999) 2845.
- [14] Arnott, W.P., Moosmüller, H. and Walker, J.W., *Rev. Sci. Instrum.* 71 (2000) 4545.
- [15] Mulholland, G.W. and Bryner, N.P., *Atmos. Environ.* 28 (1994) 873.
- [16] Abu-Rahmah, A., Arnott, W.P. and Moosmüller, H., *Meas. Sc. Technol.* 17 (2006) 1723.
- [17] Lyamani, H., Olmo, F.J. and Alados-Arboledas, L., *Atmos. Chem. Phys.* 10 (2010) 239.
- [18] Andreae, M.O., Schmid, O., Yang, H., Chand, D., Yu, J.Z., Zeng, L. and Zhang, Y., *Atmos. Environ.* 42 (2008) 6335 DOI: 10.1016/j.atmosenv.2008.01.030.
- [19] Eidels-Dubovoi, S., *The Science of Total Environment*, 287 (2002) 213.

Authors Index

Al Dahoudi Naji.....	55
Al Tahtamouni T. M.	77
Alquran M. Kh.	69
Hamasha Khadeejeh M.	83
Hijjawi R. S.....	47
Jaradat E. K.....	47
Jiang H. X.	77
Kandalyan R. A.....	69
Khalifeh J. M.	47
Lin J. Y.	77
Poopalan P.	61
Ramli N.....	61
Saif Ala'eddin A.	61
Sedhain A.....	77

Subject Index

AFM.....	61
Be-doped GaN	77
BST	61
Canonical quantization.....	47
Carbon nanotubes.....	55
Colloid	55
Coulomb gauge	47
Earthquakes.....	69
Electrical conductivity	55
Fractional derivative	47
Free electromagnetic lagrangian density.....	47
Ionosphere.....	69
ITO nanoparticles.....	55
Light absorption.....	83
Light extinction.....	83
Light scattering	83
Lorentz gauge.....	47
MOCVD epitaxial growth.....	77
<i>p</i> -type.....	77
Scintillation.....	69
Sol-gel.....	61
Space plasma.....	69
Surface roughness	61
Thin film	61
Thin films.....	55
Visibility	83

المناقشة: يجب أن تكون موجزة وتركز على تفسير النتائج.

الاستنتاج: يجب أن يكون وصفا موجزا لأهم ما توصلت إليه الدراسة ولا يزيد عن صفحة مطبوعة واحدة.

الشكر والعرفان: الشكر والإشارة إلى مصدر المنح والدعم المالي يكتبان في فقرة واحدة تسبق المراجع مباشرة.

المراجع: يجب طباعة المراجع بأسطر مزدوجة ومرقمة حسب تسلسلها في النص. وتكتب المراجع في النص بين قوسين مربعين. ويتم اعتماد اختصارات الدوريات حسب نظام Wordlist of Scientific Reviewers.

الجدول: تعطى الجداول أرقاماً متسلسلة يشار إليها في النص. ويجب طباعة كل جدول على صفحة منفصلة مع عنوان فوق الجدول. أما الحواشي التفسيرية، التي يشار إليها بحرف فوقي، فتكتب أسفل الجدول.

الرسوم التوضيحية: يتم ترقيم الأشكال والرسومات والرسومات البيانية (المخططات) والصور، بصورة متسلسلة كما وردت في النص.

تقبل الرسوم التوضيحية المستخرجة من الحاسوب والصور الرقمية ذات النوعية الجيدة بالأبيض والأسود، على أن تكون أصيلة وليست نسخة عنها، وكل منها على ورقة منفصلة ومعرفة برقمها بالمقابل. ويجب تزويد المجلة بالرسومات بحجمها الأصلي بحيث لا تحتاج إلى معالجة لاحقة، وألا تقل الحروف عن الحجم 8 من نوع Times New Roman، وألا تقل سماكة الخطوط عن 0.5 وبكثافة متجانسة. ويجب إزالة جميع الألوان من الرسومات ما عدا تلك التي ستنتشر ملونة. وفي حالة إرسال الرسومات بصورة رقمية، يجب أن تتوافق مع متطلبات الحد الأدنى من التمايز (1200 dpi Resolution) لرسومات الأبيض والأسود الخطية، و 600 dpi للرسومات باللون الرمادي، و 300 dpi للرسومات الملونة. ويجب تخزين جميع ملفات الرسومات على شكل (jpg)، وأن ترسل الرسوم التوضيحية بالحجم الفعلي الذي سيظهر في المجلة. وسواء أرسل المخطوط بالبريد أو عن طريق الشبكة (Online)، يجب إرسال نسخة ورقية أصلية ذات نوعية جيدة للرسومات التوضيحية.

مواد إضافية: تشجع المجلة الباحثين على إرفاق جميع المواد الإضافية التي يمكن أن تسهل عملية التحكيم. وتشمل المواد الإضافية أي اشتقاقات رياضية مفصلة لا تظهر في المخطوط.

المخطوط المنقح (المعدل) والأقراص المدمجة: بعد قبول البحث للنشر وإجراء جميع التعديلات المطلوبة، فعلى الباحثين تقديم نسخة أصلية ونسخة أخرى مطابقة للأصلية مطبوعة بأسطر مزدوجة، وكذلك تقديم نسخة إلكترونية تحتوي على المخطوط كاملاً مكتوباً على Microsoft Word for Windows 2000 أو ما هو استجد منه. ويجب إرفاق الأشكال الأصلية مع المخطوط النهائي المعدل حتى لو تم تقديم الأشكال إلكترونياً. وتخزن جميع ملفات الرسومات على شكل (jpg)، وتقدم جميع الرسومات التوضيحية بالحجم الحقيقي الذي ستظهر به في المجلة. ويجب إرفاق قائمة ببرامج الحاسوب التي استعملت في كتابة النص، وأسماء الملفات على قرص مدمج، حيث يعلم القرص بالاسم الأخير للباحث، وبالرقم المرجعي للمخطوط للمراسلة، وعنوان المقالة، والتاريخ. ويحفظ في مغلف واق.

الفهرسة: تقوم المجلة الأردنية للفيزياء بالإجراءات اللازمة لفهرستها وتلخيصها في جميع الخدمات الدولية المعنية.

حقوق الطبع

يُشكّل تقديم مخطوط البحث للمجلة اعترافاً صريحاً من الباحثين بأن مخطوط البحث لم يُنشر ولم يُقدّم للنشر لدى أي جهة أخرى كانت وبأي صيغة ورقية أو إلكترونية أو غيرها. ويُشترط على الباحثين ملء نموذج يُنصّ على نقل حقوق الطبع لتصبح ملكاً لجامعة اليرموك قبل الموافقة على نشر المخطوط. ويقوم رئيس التحرير بتزويد الباحثين بإنموذج نقل حقوق الطبع مع النسخة المُرسلة للتنقيح. كما ويُمنع إعادة إنتاج أي جزء من الأعمال المنشورة في المجلة من دون إذن خطي مُسبق من رئيس التحرير.

إخلاء المسؤولية

إن ما ورد في هذه المجلة يعبر عن آراء المؤلفين، ولا يعكس بالضرورة آراء هيئة التحرير أو الجامعة أو سياسة اللجنة العليا للبحث العلمي أو وزارة التعليم العالي والبحث العلمي. ولا يتحمل ناشر المجلة أي تبعات مادية أو معنوية أو مسؤوليات عن استعمال المعلومات المنشورة في المجلة أو سوء استعمالها.

معلومات عامة

المجلة الأردنية للفيزياء هي مجلة بحوث علمية عالمية مُحكمة تصدر عن اللجنة العليا للبحث العلمي، وزارة التعليم العالي والبحث العلمي، عمان، الأردن. وتقوم بنشر المجلة عمادة البحث العلمي والدراسات العليا في جامعة اليرموك، إربد، الأردن. وتُنشر البحوث العلمية الأصلية، إضافة إلى المراسلات القصيرة Short Communications، والملاحظات الفنية Technical Notes، والمقالات الخاصة Feature Articles، ومقالات المراجعة Review Articles، في مجالات الفيزياء النظرية والتجريبية، باللغتين العربية والإنجليزية.

تقديم مخطوط البحث

تُرسل نسخة أصلية وثلاث نسخ من المخطوط، مُرفقة برسالة تغطية من جانب الباحث المسؤول عن المراسلات، إلى رئيس التحرير:

أ.د. ابراهيم أبو الجرايش،

رئيس التحرير، المجلة الأردنية للفيزياء،

عمادة البحث العلمي والدراسات العليا،

جامعة اليرموك، إربد، الأردن.

هاتف : 00 962 2 72 11 111 / فرعي: 2075

فاكس : 00 962 2 72 11 121

بريد إلكتروني : jjp@yu.edu.jo

تقديم المخطوطات إلكترونياً: اتبع التعليمات في موقع المجلة على الشبكة العنكبوتية.

ويجري تحكيم البحوث الأصلية والمراسلات القصيرة والملاحظات الفنية من جانب مُحكمين اثنين في الأقل من ذوي الاختصاص والخبرة. وتُشجّع المجلة الباحثين على اقتراح أسماء المحكمين. أما نشر المقالات الخاصة في المجالات الفيزيائية النشطة، فيتم بدعوة من هيئة التحرير، ويُشار إليها كذلك عند النشر. ويُطلب من كاتب المقال الخاص تقديم تقرير واضح يتسم بالدقة والإيجاز عن مجال البحث تمهيداً للمقال. وتُنشر المجلة أيضاً مقالات المراجعة في الحقول الفيزيائية النشطة سريعة التغير، وتُشجّع كاتبها مقالات المراجعة أو مُستكثبيها على إرسال مقترح من صفحتين إلى رئيس التحرير. ويُرفق مع البحث المكتوب باللغة العربية ملخص (Abstract) وكلمات دالة (Keywords) باللغة الإنجليزية.

ترتيب مخطوط البحث

يجب أن تتم طباعة مخطوط البحث ببنط 12 نوعه Times New Roman، ويسطر مزدوج، على وجه واحد من ورق A4 (21.6 × 27.9 سم) مع حواشي 3.71 سم، باستخدام معالج كلمات ميكروسوفت وورد 2000 أو ما استُجد منه. ويجري تنظيم أجزاء المخطوط وفق الترتيب التالي: صفحة العنوان، الملخص، رموز التصنيف (PACS)، المقدمة، طرق البحث، النتائج، المناقشة، الخلاصة، الشكر والعرفان، المراجع، الجداول، قائمة بدليل الأشكال والصور والإيضاحات، ثم الأشكال والصور والإيضاحات. وتُكتب العناوين الرئيسية بخط غامق، بينما تُكتب العناوين الفرعية بخط مائل.

صفحة العنوان: وتشمل عنوان المقالة، أسماء الباحثين الكاملة وعناوين العمل كاملة. ويكتب الباحث المسؤول عن المراسلات اسمه مشاراً إليه بنجمة، والبريد الإلكتروني الخاص به. ويجب أن يكون عنوان المقالة موجزاً وواضحاً ومعبراً عن فحوى (محتوى) المخطوط، وذلك لأهمية هذا العنوان لأغراض استرجاع المعلومات.

الملخص: المطلوب كتابة فقرة واحدة لا تزيد على مائتي كلمة، موضحة هدف البحث، والمنهج المتبع فيه والنتائج وأهم ما توصل إليه الباحثون.

الكلمات الدالة: يجب أن يلي الملخص قائمة من 4-6 كلمات دالة تعبر عن المحتوى الدقيق للمخطوط لأغراض الفهرسة.

PACS: يجب إرفاق الرموز التصنيفية، وهي متوفرة في الموقع <http://www.aip.org/pacs/pacs06/pacs06-toc.html>.

المقدمة: يجب أن توضّح الهدف من الدراسة وعلاقتها بالأعمال السابقة في المجال، لا أن تكون مراجعة مكثفة لما نُشر (لا تزيد المقدمة عن صفحة ونصف الصفحة مطبوعة).

طرائق البحث (التجريبية / النظرية): يجب أن تكون هذه الطرائق موضحة بتفصيل كاف لإتاحة إعادة إجرائها بكفاءة، ولكن باختصار مناسب، حتى لا تكون تكراراً للطرائق المنشورة سابقاً.

النتائج: يستحسن عرض النتائج على صورة جداول وأشكال حيثما أمكن، مع شرح قليل في النص ومن دون مناقشة تفصيلية.

Jordan Journal of

PHYSICS

An International Peer-Reviewed Research Journal

Published by the Deanship of Research & Graduate Studies, Yarmouk University, Irbid, Jordan

Name: الأسم:
 Specialty: التخصص:
 Address: العنوان:
 P.O. Box: صندوق البريد:
 City & Postal Code: المدينة/الرمز البريدي:
 Country: القطر:
 Phone: رقم الهاتف:
 Fax No: رقم الفاكس:
 E-mail: البريد الإلكتروني:
 No. of Subscription: عدد الاشتراكات:
 Method of Payment: طريقة الدفع:
 Amount Enclosed: المبلغ المرفق:
 Signature: التوقيع:

Cheques should be paid to Deanship of Research and Graduate Studies - Yarmouk University.

I would like to subscribe to the Journal
For

- One Year
 Two Years
 Three Years

One Year Subscription Rates

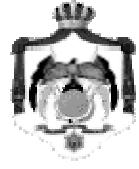
	Inside Jordan	Outside Jordan
Individuals	JD 8	€ 40
Students	JD 4	€ 20
Institutions	JD 12	€ 60

Correspondence**Subscriptions and Sales:**

Prof. Ibrahim O. Abu-AlJarayesh
 Deanship of Research and Graduate Studies
 Yarmouk University
 Irbid – Jordan
Telephone: 00 962 2 711111 Ext. 2075
Fax No.: 00 962 2 7211121



جامعة اليرموك



المملكة الأردنية الهاشمية

المجلة الأردنية
للفيزياء
مجلة بحوث علمية عالمية محكمة

المجلد (3)، العدد (2)، 2010م / 1432هـ

المجلة الأردنية
للفيزياء
مجلة بحوث علمية عالمية محكمة

المجلد (3)، العدد (2)، 2010م / 1432هـ

المجلة الأردنية للفيزياء: مجلة بحوث علمية عالمية محكمة أسستها اللجنة العليا للبحث العلمي، وزارة التعليم العالي والبحث العلمي، الأردن، وتصدر عن عمادة البحث العلمي والدراسات العليا، جامعة اليرموك، إربد، الأردن.

رئيس التحرير:

ابراهيم عثمان أبو الجرايش

قسم الفيزياء، جامعة اليرموك، إربد، الأردن.

ijaraysh@yu.edu.jo

هيئة التحرير:

ضياء الدين محمود عرفة

قسم الفيزياء، الجامعة الأردنية، عمان، الأردن.

darafah@ju.edu.jo

نديل يوسف أيوب

قسم الفيزياء، جامعة اليرموك، إربد، الأردن.

nayoub@yu.edu.jo

هشام بشارة غصيب

جامعة الأميرة سمية للتكنولوجيا، عمان، الأردن.

ghassib@psut.edu.jo

جميل محمود خليفة

قسم الفيزياء، الجامعة الأردنية، عمان، الأردن.

jkalifa@ju.edu.jo

سامي حسين محمود

قسم الفيزياء، الجامعة الأردنية، عمان، الأردن.

s.mahmood@ju.edu.jo

مروان سليمان موسى

قسم الفيزياء، جامعة مؤتة، الكرك، الأردن.

mmousa@mutah.edu.jo

نهاد عبد الرؤوف يوسف

قسم الفيزياء، جامعة اليرموك، إربد، الأردن.

nihadyusuf@yu.edu.jo

خلف عبد العزيز المساعيد

قسم الفيزياء التطبيقية، جامعة العلوم والتكنولوجيا الأردنية، إربد، الأردن.

khalaf@just.edu.jo

سكرتير التحرير: مجدي الشناق

ترسل البحوث إلى العنوان التالي:

الأستاذ الدكتور إبراهيم عثمان أبو الجرايش
رئيس تحرير المجلة الأردنية للفيزياء
عمادة البحث العلمي والدراسات العليا، جامعة اليرموك
إربد، الأردن

هاتف 00 962 2 7211111 فرعي 2075

E-mail: jjp@yu.edu.jo

Website: <http://Journals.yu.edu.jo/jjp>

